

Self-configuring feedback loops for sensorimotor control

Sergio Verdúzco-Flores^{1,2} and Erik De Schutter¹

¹Computational Neuroscience Unit, OIST

²Neural Computation Unit, OIST

Abstract

How dynamic interactions between nervous system regions in mammals performs online motor control remains an unsolved problem. In this paper we show that feedback control is a simple, yet powerful way to understand the neural dynamics of sensorimotor control. We make our case using a minimal model comprising spinal cord, sensory and motor cortex, coupled by long connections that are plastic. It succeeds in learning how to perform reaching movements of a planar arm with 6 muscles in several directions from scratch. The model satisfies biological plausibility constraints, like neural implementation, transmission delays, local synaptic learning and continuous online learning. The model can go from motor babbling to reaching arbitrary targets in less than 10 minutes of *in silico* time. Movements are ataxic, as in a motor system without a cerebellum. As emergent properties, neural populations in motor cortex show directional tuning and oscillatory dynamics, and the spinal cord creates convergent force fields that add linearly. Successful variations of the model have one trait in common: configuration of feedback control through differential Hebbian plasticity rules.

1 Introduction

1.1 The challenge

Neuroscience has made great progress in decoding how cortical regions perform specific brain functions like primate vision [1, 2] and rodent navigation [3, 4]. Conversely, the evolutionary much older motor control system still poses fundamental questions, despite a large body of experimental work. This is because, in mammals, in addition to areas in cortex like premotor and motor areas and to some degree sensory and parietal ones, many *extracortical regions* have important and unique functions: basal ganglia, thalamus, cerebellum, pons, brain stem nuclei like the red nucleus and spinal cord [5, 6]. These structures are highly interconnected by fast conducting axons and all show strong dynamic

activity changes, related to the ongoing dynamics of the performed motor act. Clinical and lesion studies have confirmed the necessity of each of these regions for normal smooth motor control of arm reaching [7, 8].

Fully understanding motor control will thus entail understanding the simultaneous function and interplay of all brain regions involved. Little by little, new experimental techniques will allow us to monitor more neurons, in more regions, and for longer periods [9, e.g.]. But to make sense of these data computational models must step up to the task of integrating all those regions to create a functional neuronal machine.

Finally, relatively little is known about the neural basis of motor development *in infants* [10]. Nevertheless, a full understanding of primate motor control will not only require explanation of how these brain regions complement and interact with each other but also how this can be learned during childhood.

With these challenges in mind we recently developed a motor control framework based on differential Hebbian learning [11]. A common theme in physiology is the control of *homeostatic variables* (e.g. blood glucose levels, body temperature, etc.) using negative feedback mechanisms [12]. From a broad perspective, our approach considers the musculoskeletal system as an extension of this homeostatic control system: movement aims to make the external environment conducive to the internal control of homeostatic variables (e.g. by finding food, or shelter from the sun).

Our working hypothesis is that motor cortex sends downstream signals to correct errors in the desired value of higher-level variables. This involves a feedback control loop that minimally contains motor cortex, the spinal cord, and sensory cortex. We will show that a properly configured control loop has the potential to explain many experimental phenomena, even when plasticity is absent in the model. We further show that the plasticity rules in [11] can explain how the control loop can arise.

1.2 Relevant findings in motor control

Before describing our modeling approach, we summarize some of the relevant experimental data that will be important to understanding the results. We focus on three related issues: 1) the role of the spinal cord in movement, 2) the nature of representations in motor cortex, and 3) muscle synergies, and how the right pattern of muscle activity is produced.

For animals to move, spinal motoneurons must activate the skeletal muscles. In general, descending signals from the corticospinal tract do not activate the motoneurons directly, but instead provide input to a network of excitatory and inhibitory interneurons [13, 14, 15, 16, 17, 18, 19, 20]. Learning even simple behaviors involves long-term plasticity, both at the spinal cord (SC) circuit, and at higher regions of the motor hierarchy [21, 22, 23, 24, 25]. Despite its obvious importance, there are comparatively few attempts to elucidate the nature of the SC computations, and the role of synaptic plasticity.

The role ascribed to SC is closely related to the role assumed from motor cortex, particularly M1. One classic result is that M1 pyramidal neurons of

macaques activate preferentially when the hand is moving in a particular direction. When the preferred directions of a large population of neurons are added as vectors, a population vector appears, which points close to the hand’s direction of motion [26, 27]. This launched the hypothesis that M1 represents kinematic, or other high-level parameters of the movement, which are transformed into movements in concert with the SC. This hypothesis mainly competes with the view that M1 represents muscle forces. Much research has been devoted to this issue [28, 29, 30, 31, 32, 33, 34, 35, e.g.].

Another important observation is that the preferred directions of motor neurons cluster around one main axis. As shown in [36], this suggests that M1 is mainly concerned with dynamical aspects of the movement, rather than representing its kinematics.

A related observation is that the preferred directions in M1 neurons experience random drifts that overlap learned changes [37, 38]. This leads to the hypothesis that M1 is a redundant network that is constantly using feedback error signals to capture the *task-relevant dimensions*, placing the configuration of synaptic weights in an *optimal manifold*.

A different perspective for studying motor cortex is to focus on how it can produce movements, rather than describing its activity [39]. One specific proposal is that motor cortex has a collection of pattern generators, and specific movements can be created by combining their activity [39, 40]. Experimental support for this hypothesis came through the surprising finding of rotational dynamics in motor cortex activity [41], suggesting that oscillators with different frequencies are used to produce desired patterns. This begs the question of how the animal chooses its desired patterns of motion.

Selecting a given pattern of muscle activation requires *planning*. Motor units are the final actuators in the motor system, but they number in the tens of thousands, so planning movements in this space is unfeasible. A low-dimensional representation of desired limb configurations (such as the location of the hand in Euclidean coordinates) is better. Movement generation likely involves a coordinate transformation, from the endpoint coordinates (e.g. hand coordinates) into actuator coordinates (e.g. muscle lengths), from which motor unit activation follows directly. Even using pure engineering methods, as for robot control, computing this coordinate transformation is very challenging. For example, this must overcome kinematic redundancies, as when many configurations of muscle lengths put the hand in the same location.

The issue of coordinate transformation is central for motor control [7, 42, 43]; *motor primitives and muscle synergies* are key concepts in this discussion. Representing things as combinations of elementary components is a fundamental theme in applied mathematics. For example, linear combinations of basis vectors can represent any vector, and linear combinations of wavelets can approximate any smooth function [44]. In motor control, this idea arises in the form of motor primitives. Motor primitives constitute a set of basic motions, such that any movement can be decomposed into them [45, 46, 47]. This is closely related to the concept of synergies. The term “synergy” may mean several things [48, 49], but in this paper we use it to denote a pattern of muscle activity arising as a

coherent unit. Synergies may be composed of motor primitives, or they may be the motor primitives themselves.

A promising candidate for motor primitives comes in the form of convergent force fields, which have been observed for the hindlimbs of frogs and rats [50, 51], or in the forelimbs of monkeys [52]. In experiments where the limb is held at a particular location, local stimulation of the spinal cord will cause a force to the limb’s endpoint. The collection of these force vectors for all of the limb endpoint’s positions forms a force field, and these force fields have two important characteristics: 1) they have a unique fixed point, and 2) simultaneous stimulation of two spinal cord locations produces a force field which is the sum of the force fields from stimulating the two locations independently. It is argued that movement planning may be done in terms of force fields, since they can produce movements that are resistant to perturbations, and also permit a solution to the problem of coordinate transformation with redundant actuators [46].

The neural origin of synergies, and whether they are used by the motor system is a matter of ongoing debate [53, 54, 55]. To us, it is of interest that single spinal units found in the mouse [56] and monkey [57] spinal cord (sometimes called Motor Synergy Encoders, or MSEs) can reliably produce specific patterns of motoneuron activation.

1.3 Model concepts

We believe that it is impossible to understand the complex dynamical system in biological motor control without the help of computational modeling. Therefore we set out to build a minimal model that could eventually control an autonomous agent, while still satisfying biological plausibility constraints.

Design principles and biological-plausibility constraints for neural network modeling have been proposed before [58, 59, 60]. Placing emphasis on the motor system, we compiled a set of characteristics that cover the majority of these constraints. Namely:

- **Spanning the whole sensorimotor loop.**
- **Using only neural elements. Learning their connection strengths is part of the model.**
- **Learning does not rely on a training dataset. It is instead done by synaptic elements using local information.**
- **Learning arises from continuous-time interaction with a continuous-space environment.**
- **There is a clear vision on how the model integrates with the rest of the brain in order to enact more general behavior.**

Our aim is hierarchical control of homeostatic variables, with the spinal cord and motor cortex at the bottom of this hierarchy. At first glance, spinal plasticity poses a conundrum, because it changes the effect of corticospinal inputs.

Cortex is playing a piano that keeps changing its tuning. A solution comes when we consider the corticospinal loop (e.g. the long-loop reflex) as a negative control system, where the spinal cord activates the effectors to reduce an error. The role of cortex is to produce perceptual variables that are controllable, and can eventually improve homeostatic regulation. In this regard, our model is a variation of Perceptual Control Theory [61, 62], but if the desired value of the controller is viewed as a prediction, then this approach resembles active inference models [63]. Either way, the goal of the system is to reduce the difference between the desired and the perceived value of some variable.

If cortex creates representations for perceptual variables, the sensorimotor loop must be configured so those variables can be controlled. This happens when the error in those variables activates the muscles in a way that brings the perceived value closer to the desired value. In other words, we must find the input-output structure of the feedback controller implicit in the long-loop reflex. We have found that this important problem can be solved by the differential Hebbian learning rules introduced in [11]. We favor the hypothesis that this learning takes place is in the connections from motor cortex to interneurons and brainstem. Nevertheless, we show that all our results are valid if learning happens in the connections from sensory to motor cortex.

In the Results section we will describe our model, its variations, and how it can learn to reach. Next we will show that many phenomena described in section 1.2 are present in this model. These phenomena emerge from having a properly configured neural feedback controller with a sufficient degree of biological realism. This means that even if the synaptic weights of the connections are set by hand and static, the phenomena still emerge, as long as the system is configured to reduce errors. In short, we show that a wealth of phenomena in motor control can be explained simply by feedback control in the sensorimotor loop, and that this feedback control can be configured in a flexible manner by the learning rules presented in [11].

2 Results

2.1 A neural architecture for motor control

The model in this paper contains the main elements of the long-loop reflex, applied to the control of a planar arm using six muscles. The left panel of figure 1 shows the architecture of the model, which contains 74 firing rate neurons organized in six populations. This architecture resembles a feedback controller that makes the activity in a neural population S_A approach the activity in a different population S_P .

The six firing-rate neurons (called *units* in this paper) in S_A represent a region of somatosensory cortex, and its inputs consist of the static gamma (II) afferents. In steady state, activity of the II afferents is monotonically related to muscle length [64], which in turn can be used to prescribe hand location. Other afferent signals are not provided to S_A in the interest of simplicity.

S_P represents a different cortical layer of the same somatosensory region as S_A , where a “desired” or “predicted” activity has been caused by brain regions not represented in the model. Each firing rate neuron in S_A has a corresponding unit in S_P , and they represent the mean activity at different levels of the same microcolumn [65]. S_{PA} is a region (either in sensory or motor cortex) that conveys the difference between activities in S_P and S_A , which is the error signal minimized by negative feedback control.

Population A represents sensory thalamus and dorsal parts of the spinal cord. It contains 18 units with logarithmic activation functions, each receiving an input from a muscle afferent. Each muscle provides proprioceptive feedback from models of the Ia, Ib, and II afferents. In rough terms, Ia afferents provide information about contraction velocity, and Ib afferents signal the amount of tension in the muscle and tendons.

Population M represents motor cortex. Ascending inputs to M arise from population A , and use a variation of the *input correlation* learning rule [66], where the S_{PA} inputs act as a learning signal. The input correlation rule enhances the stability of the controller. More details are presented in Methods. The S_{PA} inputs to M can either be static, or use a learning rule to be described below.

To represent excitatory and inhibitory neuron populations, both M and S_{PA} use a “dual representation”, where each error signal is represented by two units. Let $e_i = s_P^i - s_A^i$ be the error associated with the i -th muscle. One of the two S_{PA} units representing e_i is a monotonic function of $\max(e_i, 0)$, whereas the other unit increases according to $\max(-e_i, 0)$. These opposing inputs, along with mutual inhibition between the two units creates dynamics where sensorimotor events cause both excitatory and inhibitory responses, which agrees with experimental observations [67, 68, 69], and allows transmitting “negative” values using excitatory projections. Dual units in M receive the same inputs, but with the opposite sign.

The task of specifying which muscles should be activated in order to reduce S_{PA} errors can be done in one of two locations according to the configuration of the model. In a first configuration, called “configuration 1” in this paper, the task is performed by a “spinal” network C that transforms the M outputs into muscle stimulation. C learns to transform sensory errors into appropriate motor commands using a differential Hebbian learning rule [11]. In this configuration the error input to each M unit comes from one of the S_{PA} activities. Alternatively, in the “configuration 2” S_{PA} sends “all-to-all” connections to M using the differential Hebbian rule, whereas the connections from M to C use appropriately patterned static connections. A third configuration (“configuration 3”) uses hand-set static connections approximating the optimal solution everywhere (See Methods, 4.5).

We explain the idea behind the differential Hebbian rule as applied in the connections from M to C . C contains N interneurons, whose activity vector we denote as $\mathbf{c} = [c_1, \dots, c_N]$. The input to each of these units is an M -dimensional vector $\mathbf{e} = [e_1, \dots, e_M]$. Each unit in C has an output $c_i = \sigma\left(\sum_j \omega_{ij} e_j\right)$, where

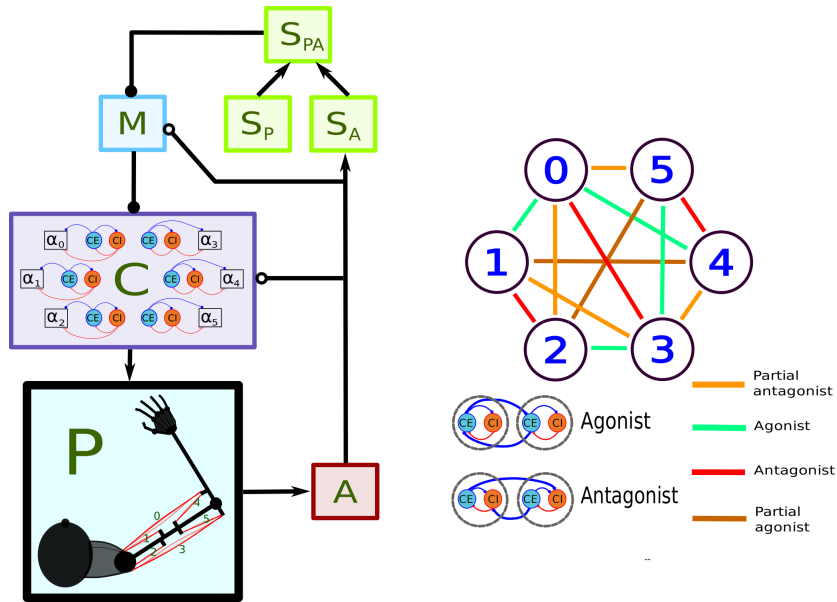


Figure 1: Main components of the model. In the left panel each box stands for a neural population, except for **P**, which represents the arm and the muscles. Arrows indicate static connections, open circles show *input correlation* synapses, and filled circles show possible locations of synapses with the learning rule in [11]. Only one of the filled circles will have plastic synapses. **A**: afferent population. **S_A**: Somatosensory cortex, modulated by afferent input. **S_P**: somatosensory cortex, prescribed pattern. **S_{PA}**: population signaling the difference between **S_P** and **S_A**. **M**: primary motor cortex. **C**: spinal cord. Inside the **C** box the circles represent the excitatory (**CE**) and inhibitory (**CI**) interneurons, organized into six pairs. The interneurons in each pair innervate an alpha motoneuron (α), each of which stimulates one of the six muscles in the arm, numbered from 0 to 5. The trios consisting of **CE**, **CI**, α units are organized into agonists and antagonists, depending on whether their α motoneurons cause torques in similar or opposite directions. These relations are shown in the right-side panel.

$\sigma(\cdot)$ is a positive sigmoidal function. The inputs are assumed to be errors, and to reduce them we want e_j to activate c_i when c_i can reduce e_j . One way this could happen is when the weight ω_{ij} from e_j to c_i is proportional to the negative of their sensitivity derivative:

$$\omega_{ij} \propto -\frac{\partial e_j}{\partial c_i}. \quad (1)$$

Assuming a monotonic relation between the motor commands and the errors, relation 1 entails that errors will trigger an action to cancel them, with some caveats considered in [11]. Synaptic weights akin to equation 1 can be obtained using a learning rule that extracts correlations between the derivatives of c_i and e_j (see Methods). Using this rule, the commands coming from population C can eventually move the arm so that S_A activity resembles S_P activity.

C is organized to capture the most basic motifs of spinal cord connectivity using a network where balance between excitation and inhibition is crucial [70, 71, 72]. Each one of six α motoneurons stimulate one muscle, and is stimulated by one excitatory (CE), and one inhibitory (CI) interneuron. CE and CI stimulate one another, resembling the classic Wilson-Cowan model [73]. The trios composed of α, CE , and CI neurons compose a group that controls the activation of one muscle, with CE and CI receiving convergent inputs from M . This resembles the premotor network model in [74]. (α, CE, CI) trios are connected to other trios following the agonist-antagonist motif that is common in the spinal cord [75]. This means that CE units project to the CE units of agonists, and to the CI units of antagonists (figure 1, right panel). When the agonist/antagonist relation is not strongly defined, muscles can be ‘partial’ agonists/antagonists, or unrelated.

Connections from A to C (the “short-loop reflex”) use the input correlation learning rule, analogous to the connections from A to M .

Direct connections from M to alpha motoneurons are not necessary for the model to reach, but they were introduced in new versions because in higher primates these connections are present for distal joints [14]. Considering that bidirectional plasticity has been observed in corticomotoneural connections [76], we chose to endow them with the differential Hebbian rule of [11].

Because timing is essential to support the conclusions of this paper, every connection has a transmission delay, and all firing rate neurons are modeled with ordinary differential equations.

All the results in this paper apply to the 3 configurations described above (1:learning in the spinal cord, 2:learning in motor cortex, 3:static connections), plus two additional configurations (explained below) derived from configuration 1.

There is evidence for interneurons that drive a set of muscles, possibly setting the circuit foundation for motor synergies [45, 55, 56]. Configuration 4 explores whether reaching can be learned when the CE and CI units send projections to more than one motoneuron. To achieve this we modified the architecture of figure 1 so that for every combination of two different muscles there was a pair of CE, CI units that stimulated both of them (see Methods, 4.5).

In configurations 1-4 the projections from S_{PA} to M use one-to-one connectivity (each M unit controls the length error of one muscle). Interestingly, this is not necessary. In configuration 5 each unit in M can be driven by a linear combination of S_{PA} errors, still preserving the results of this paper. Not all connection matrices between S_{PA} and M lead to the same performance, and this has not been systematically explored (see Methods, section 4.5.) Still, configuration 5 further highlights the flexibility of the learning mechanism, which may offer a new perspective on how control can arise in the face of convergent and redundant sensorimotor loops [77].

Since most results apply to all configurations, and since results could depend on the random initial weights, we report simulation results using 5 means and 5 standard deviations (mean1 \pm SD1, ..., mean5 \pm SD5), with the understanding that these 5 value pairs correspond to configurations 1, 2, 3, 4, 5 respectively, and that the statistics come from 20 independent simulations with different initial conditions. Section 8 in the Supplementary Information is provided as a quick reference to compare the numerical results for the different configurations, and to remember their basic traits.

For each configuration, a single simulation was used to produce all the representative plots in different sections of the paper.

2.2 The model can reach by matching perceived and desired sensory activity

Reaches are performed by specifying an S_P pattern equal to the S_A activity when the hand is at the target. The acquisition of these S_P patterns is not in the scope of this paper (but see [11]).

We created a set of random targets by sampling uniformly from the space of joint angles. Using this to set a different pattern in S_P every 40 seconds, we allowed the arm to move freely during 16 S_P target presentations. To produce exploratory movements we used noise (in the CE , CI units for configurations 1, 4, 5, or in the M units for configuration 2), plus two additional units described in the Methods (section 4.3), called ACT , and CHG . ACT is a leaky integrator of the total activity in S_{PA} , reflecting the total error, and triggers adaptation in CE and CI (or in M) when a threshold is crossed. CHG is connected to ACT in order to reset its activity when a new target is presented.

For all five configurations the system was capable of reaching. To decide if reaching was learned in a trial we took the average distance between the hand and the target (the *error*) during the last 4 target presentations. Learning was achieved when this error was smaller than 10 cm.

The system learned to reach in 99 out of 100 trials (20 for each configuration). One simulation for configuration 1 had an average error of 14 cm during the last 4 reaches of training. To assess the speed of learning we recorded the average number target presentations required before the error became less than 10 cm for the first time. This average number of failed reaches before the first success was: (1.8 \pm 2, 1.2 \pm .9, 0 \pm 0, 1.6 \pm 1.3, 4 \pm 2.5).

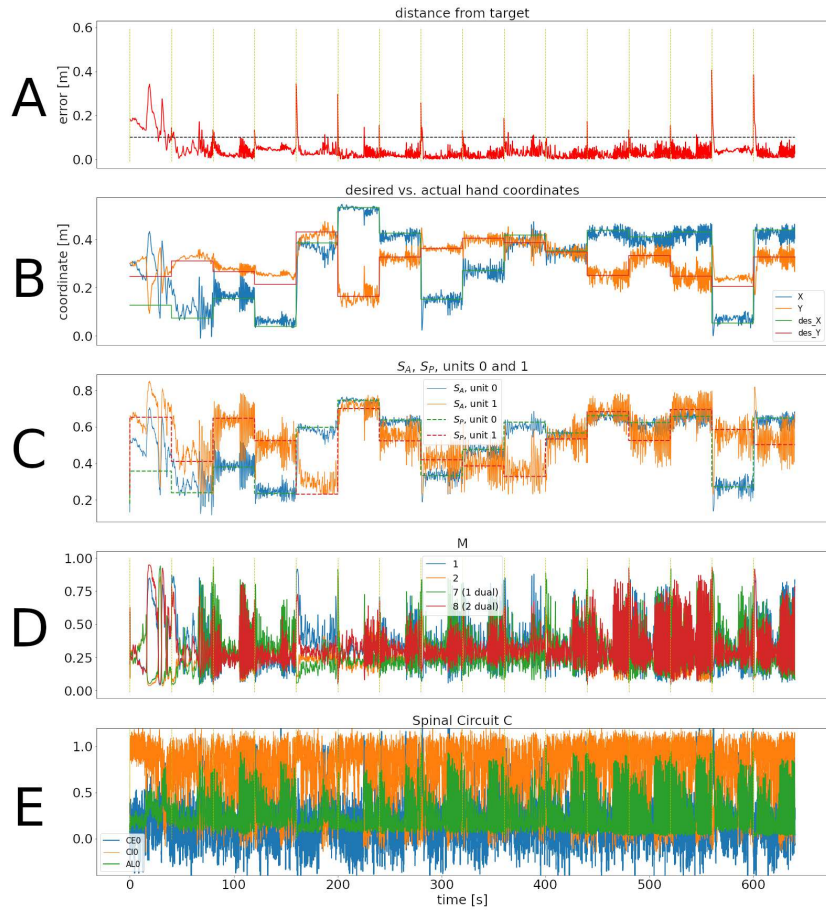


Figure 2: Representative training phase of the simulation for configuration 1. **A:** Distance between the target and the hand through 640 seconds of simulation, corresponding to 16 reaches to different targets. The dotted line corresponds to 10 centimeters. The times when S_P changes are indicated with a vertical, dotted yellow line. **B:** Desired versus actual hand coordinates through the training phase. **C:** Activity of units 0 and 1 in S_P and S_A . **D:** Activity of M units 1, 2, and their duals. **E:** Activity of the CE, CI, α trio for muscle 0.

Figure 2A shows the error through 16 successive reaches (640 seconds of *in silico* time) in a typical case for configuration 1. A supplementary video shows the arm’s movements during this simulation. Figures similar to figure 2 can be seen for all configurations in the Supplementary Information.

In figure 2A the error increases each time a new target was presented (yellow vertical lines), but as learning continues it was consistently reduced below 10 centimeters.

Panel B also shows the effect of learning, as the hand’s Cartesian coordinates eventually track the target coordinates whenever they change. This is also reflected as the activity in S_A becoming similar to the activity in S_P (panel C).

Panels D and E of figure 2 show the activity of a few units in population M and population C during the 640 seconds of this training phase. During the first few reaches, M shows a large imbalance between the activity of units and their duals, reflecting larger errors. Eventually these activities balance out, leading to a more homogeneous activity that may increase when a new target appears. M1 activation patterns that produce no movement are called the *null-space activity* [78]. In our case, this includes patterns where M units have the same activity as their duals. This, together with the noise and oscillations intrinsic to the system cause the activity in M and C to never disappear.

In panel E the noise in the C units becomes evident. It can also be seen that inhibition dominates excitation (due to CE to CI connections), which promotes stability in the circuit.

Figures analogous to figure 2 for the other 4 configurations can be found in Supplementary section 12.

We tested whether any of the novel elements in the model were superfluous. To this end, we removed each of the elements individually and checked if the model could still learn to reach. In conclusion, removing individual elements generally deteriorated performance, but the factor that proved essential for all configurations with plasticity was the differential Hebbian learning in the connections from M to C or from S_{PA} to M . Details are presented in the Supplementary Information (section 7).

2.3 Center-out reaching 1: The reach trajectories present traits of cerebellar ataxia

In order to compare our model with experimental data, after the training phase we began a standard center-out reaching task. Switching the task merely consisted of presenting the targets in a different way, but for the sake of smoother trajectories we removed the noise from the units in C or M . The noise causes random variations in the hand’s trajectory, but it does not impair reaching.

Figure 3A shows the 8 peripheral targets around a hand rest position. Before reaching a peripheral target, a reach to the center target was performed, so the whole experiment was a single continuous simulation controlled by the S_P pattern.

Peripheral targets were selected at random, each appearing 6 times. This produced 48 reaches (without counting reaches to the center), each one lasting

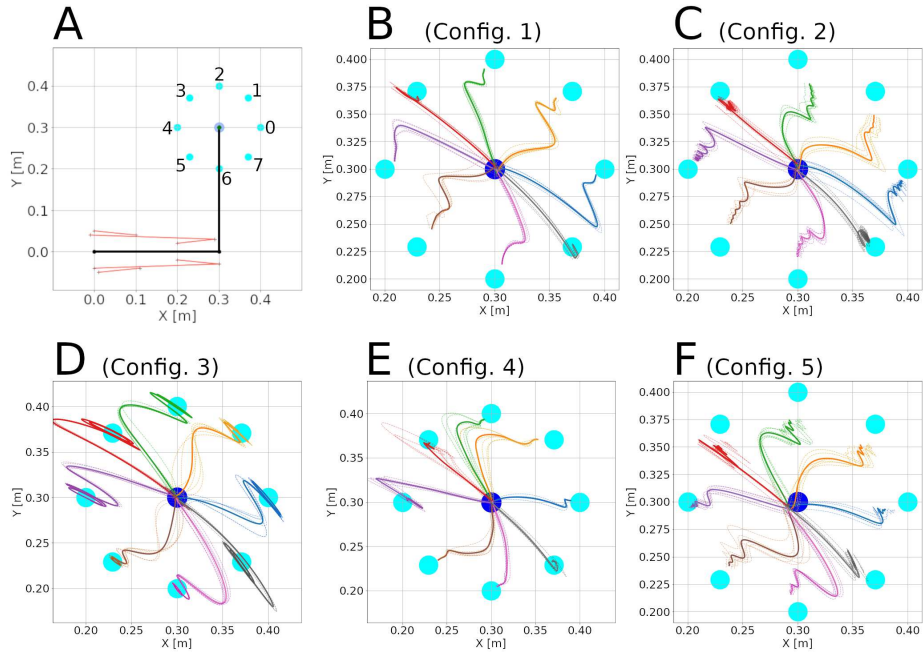


Figure 3: Center-out reaching. **A:** The arm at its resting position, with hand coordinates (0.3, 0.3) meters, where a center target is located. Eight peripheral targets (cyan dots) were located on a circle around the center target, with a 10 cm radius. The muscle lines, connecting the muscle insertion points, are shown in red. The shoulder is at the origin, whereas the elbow has coordinates (0.3, 0). Shoulder insertion points remain fixed. **B-F:** Hand trajectories for all reaches in the 5 configurations. The trajectory's color indicates the target. Dotted lines show individual reaches, whereas thick lines indicate the average of the 6 reaches.

5 seconds. Panels B through F of figure 3 show the trajectories followed by the hand in the 5 configurations. During these 48 reaches the average distance between the hand and the target was $(3.3 \pm .01, 2.9 \pm .001, 2.9 \pm .0003, 3 \pm .008, 2.8 \pm .0007)$ centimeters.

Currently our system has neither cerebellum nor visual information. Lacking a “healthy” model to make quantitative comparisons, we analyzed qualitative properties of the trajectories.

For the sake of stability and simplicity, our system is configured to perform slow movements. Fast and slow reaches are different in cerebellar patients [79]. Slow reaches undershoot the target, follow longer hand paths, and show movement decomposition (joints appear to move one at a time). In figure 3 the trajectories begin close to the 135-degree axis, indicating a slower response at the elbow joint. Some of these trajectories (e.g. Configs. 1 and 5) tend to undershoot the target, whereas others (Configs. 2 and 3) can oscillate around the target.

The traits of the trajectories can be affected by many hyperparameters in the model, but the dominant factor seems to be the gain in the control loop. Our model involves delays, activation latencies, momentum, and interaction torques. Unsurprisingly, increasing the gain will lead to oscillations along with faster reaching. On the other hand, low gain leads to slow, stable reaching that often undershoots the target. Since we do not have a cerebellum to overcome this trade off, the gain was the only hyperparameter that was manually adjusted for the 5 configurations (See Methods, section 4.7). In particular, we adjusted the slope of the M and S_A units so the system was stable, but close to the onset of oscillations. Supplementary section 9 shows examples of our configurations with higher gain and oscillations.

The shape of the trajectory also depends on the target. Different reach directions cause different interaction forces, and encounter different levels of viscoelastic resistance from the muscles.

Figure 4 reveals that the approach to the target is initially fast, but gradually slows down. Healthy subjects usually present a bell-shaped velocity profile, with some symmetry between acceleration and deceleration. This symmetry is lost with cerebellar ataxia [80, 81].

We are not aware of center-out reaching studies for cerebellar patients in the dark, but [82] does examine reaching in these conditions. Summarizing its findings:

1. Movements were slow.
2. The endpoints had small variation, but they had constant errors.
3. Longer, more circuitous trajectories, with most changes in direction during the last quarter.
4. Trajectories to the same target showed variations.

From figures 3 and 4 we can observe constant endpoint errors, except in configuration 3, which has higher gain and oscillations. Circuitous trajectories

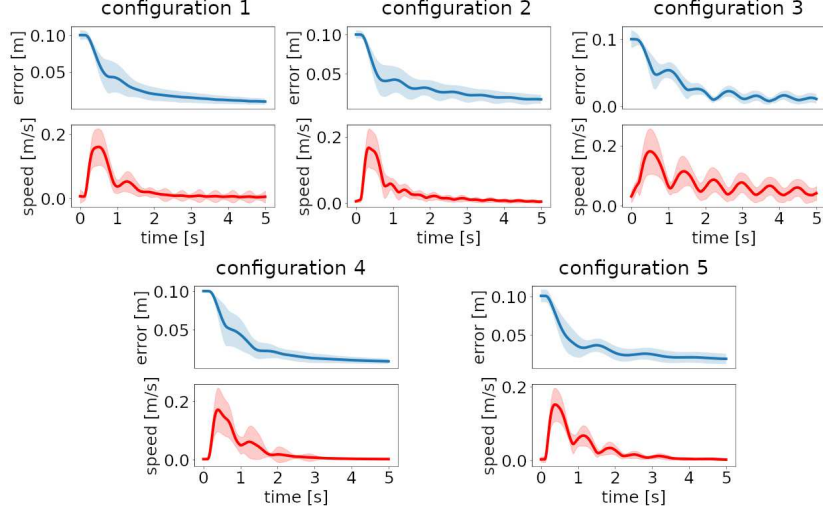


Figure 4: Distance to target and reach velocity through time for the 5 configurations. Thick lines show the average over 48 reaches (8 targets, 6 repetitions). Filled stripes show standard deviation.

with a pronounced turn around the end of the third quarter are also observed. Individual trajectories can present variations. A higher gain can increase these variations (See supplementary section 9)

2.4 Center-out reaching 2: Directional tuning and preferred directions

To find whether directional tuning could arise during learning, we analyzed the M population activity for the 48 radial reaches described in the previous subsection.

For each of the 12 units in M , figure 5A shows the mean firing rate of the unit when reaching each of the 8 targets. The red arrows show the Preferred Direction (PD) vectors that arise from these distributions of firing rates. For the sake of exposition, figure 5 shows data for the simpler case of one-to-one connectivity between S_{PA} and M (configuration 1), but these results generalize.

We found that $(11.8 \pm .4, 12 \pm 0, 12 \pm 0, 12 \pm 0, 12 \pm 0)$ units were significantly tuned to reach direction ($p < 0.001$, bootstrap test), with PD vectors of various lengths. The direction of the PD vectors is not mysterious. Each M unit controls the length error of one muscle. Figure 5B shows that the required contraction length depends on both the target and the muscle. The PD vectors of units 0-5 point to the targets that require the most contraction of their muscle. Units 6-11 are the duals of 0-5, and their PD is in the opposite direction. Figure 5C shows that the PD may also be inferred from the muscle activity, reflected as average tension.

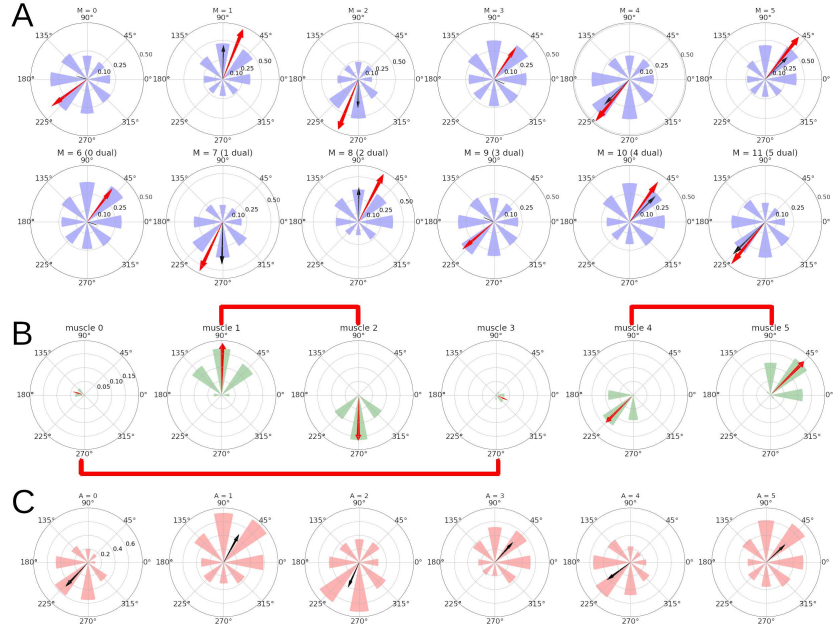


Figure 5: Directional tuning of the units in M for a simulation with configuration 1. **A:** Average firing rate per target, and preferred direction (see Methods) for each of the 12 units in M . Each polar plot corresponds to a single unit, and each of the 8 purple wedges corresponds to one of the 8 targets. The length of a wedge indicates the mean firing rate when the hand was reaching the corresponding target. The red arrow indicates the direction and relative magnitude of the PD vector. The black arrow shows the predicted PD vector, in this case just the corresponding arrows from panel B. **B:** For each muscle and target, a wedge shows the muscle's length at rest position minus the length at the target, divided by the rest position length. The red arrow comes from the sum of the wedges taken as vectors, and represents the muscle's direction of maximum contraction. Plots corresponding to antagonist muscles are connected by red lines. **C:** Average activity of the 6 A units indicating muscle tension. The arrows come from the sum of wedges taken as vectors.

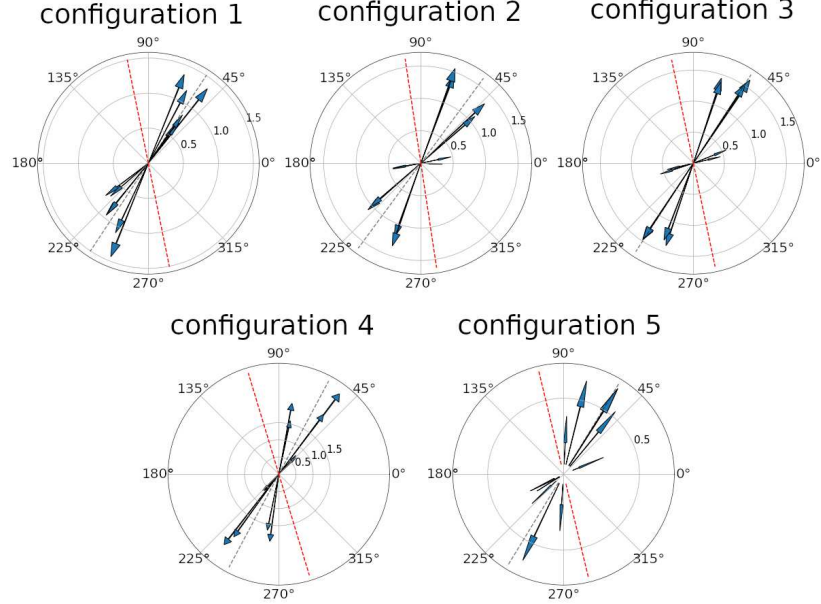


Figure 6: Preferred direction vectors for the 12 M units in all configurations. The gray dotted line shows the main axis of the distribution. The red dotted line is a 45-degree rotation the gray line, for comparison with [36].

In the case when each M unit receives a linear combination of S_{PA} errors (configuration 5), its PD can be predicted using a linear combination of the “directions of maximum contraction” shown in figure 5B, using the same weights as the S_{PA} inputs. When accounting for the length of the PD vectors, this can predict the PD angle with a coefficient of determination $R^2 \approx (.74 \pm .18, .88 \pm .14, .86 \pm .01, .89 \pm .06, .82 \pm .03)$.

As mentioned in the Introduction, the PDs of motor cortex neurons tend to align in particular directions [36]. This is almost trivially true for this model, since the PD vectors are mainly produced by linear combinations of the vectors in figure 5B.

Figure 6 shows the PD for all the M units in a representative simulation for each of the configurations. In each one of our 100 simulations the PD distribution showed significant bimodality ($p < 0.001$). The main axis of the PD distribution (see Methods) was $(59 \pm 7, 52 \pm 2, 54 \pm .5, 60 \pm 3, 58 \pm 1)$ degrees.

To compare with [36] we rotate this line 45 degrees so the targets are in the same position relative to the shoulder (e.g. [83] Fig. 1, [84] Fig. 1). This places the average main axes above in a range between 99 and 105 degrees, comparable to the 117 degrees in [36].

The study in [83] suggested that a rudimentary spinal cord feedback system should be used to understand *why* the PD distribution arises. Our model is the first to achieve this.

The PD vectors are not stationary, but experience random fluctuations that become more pronounced in new environments [37, 38]. The brain is constantly remodeling itself, without losing the ability to perform its critical operations [85]. Our model is continuously learning, so we tested the change in the PDs by setting 40 additional center-out reaches (no intrinsic noise) after the previous experiment, once for each configuration.

To encourage changes we set 10 different targets instead of 8. After a single trial for each configuration the change in angle for the 12 PD vectors had means and standard deviations of $(3.3 \pm 2.4, 4.9 \pm 2.1, .3 \pm .2, 1.8 \pm 1.3, 7 \pm 6)$ degrees. We also measured the change in the preferred directions of the muscles, obtained as in figure 5C. This yielded differences and standard deviations $(3.8 \pm 2.1, 6.4 \pm 2.9, .2 \pm .2, 11.4 \pm 15.2, 27.7 \pm 34.5)$ degrees.

The average distance between hand and target during the 40 reaches was $(3, 3.6, 2.9, 2.6, 4.5)$ cm, showing that the hand was still moving towards the targets, although with different errors due to their new locations.

Using a dynamical systems perspective, [39] considers that the muscle activity $\mathbf{m}(t)$ (a vector function of time) arises from the cortical activity vector $\mathbf{r}(t)$ after it is transformed by the downstream circuitry:

$$\mathbf{m}(t) = G[\mathbf{r}(t)]. \quad (2)$$

It is considered that the mapping $G[\cdot]$ may consist of sophisticated controllers, but for the sake of simplicity this mapping is considered static, omitting spinal cord plasticity. The cortical activity arises from a dynamical system:

$$\tau \dot{\mathbf{r}}(t) = h(\mathbf{r}(t)) + \mathbf{u}(t), \quad (3)$$

where $\mathbf{u}(t)$ represents inputs to motor cortex from other areas, and $h(\cdot)$ is a function that describes how the state of the system evolves.

A difficulty associated with equation 3 is explaining how $\mathbf{r}(t)$ generates a desired muscle pattern $\mathbf{m}(t)$ when the function $h(\cdot)$ represents the dynamics of a recurrent neural network. One possibility is that M1 has intrinsic oscillators of various frequencies, and they combine their outputs to shape the desired pattern. This prompted the search for oscillatory activity in M1 while macaques performed center-out reaching motions. A brief oscillation (in the order of 200 ms, or 5 Hz) was indeed found in the population activity [41], and the model in [40] was able to reproduce this result, although this was done in the open-loop version of equations 2 and 3, where $\mathbf{u}(t)$ contains no afferent feedback (this is further commented in the Supplemental Discussion, section 6.1).

Recently it was shown that the oscillations in motor cortex can arise when considering the full sensorimotor loop, without the need of recurrent connections in motor cortex [86]. A natural question is whether our model can also reproduce the oscillations in [41] without requiring M1 oscillators or recurrent connections.

The central part of the analysis in [41] is obtaining the first two jPCA vectors, as they define the plane of strongest rotations. Informally, this means that when the firing rate vector $\mathbf{m}(t)$ of M1 is projected onto this plane, the resulting trajectories show the most rotations.

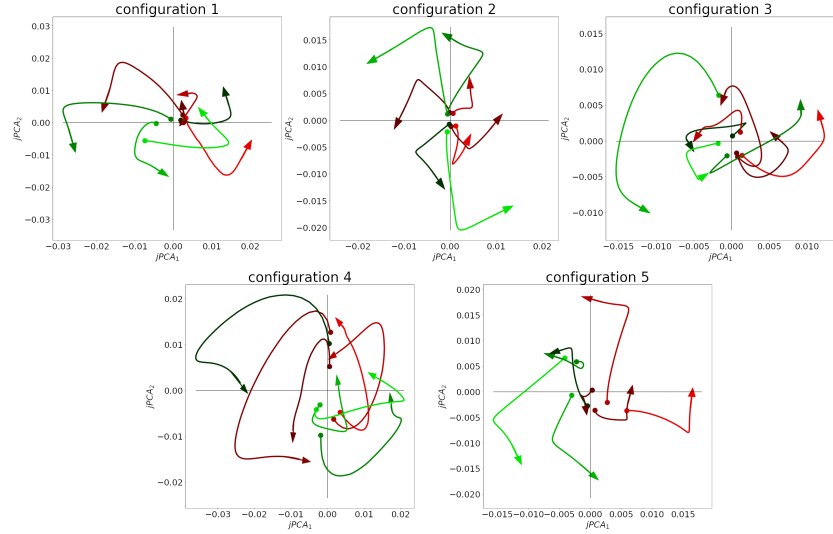


Figure 7: Rotational dynamics in the M population in a representative simulation for all configurations. Each plot shows the first two jPCA components during 0.25 seconds, for each of the 8 conditions/targets. Traces are colored according to the magnitude of their initial $jPCA_1$ component, from smallest (green) to largest (red).

Considering that we have a low-dimensional, non-spiking, slow-reaching model, we can only expect to qualitatively replicate the essential result in [41], which is most of the variance being contained in the first jPCA plane.

We replicated the jPCA analysis, with adjustments to account for the smaller number of neurons, the slower dynamics, and the fact that there is no delay period before the reach (See Methods 4.6). The result can be observed in figure 7, where 8 trajectories are seen in the plots. Each trajectory is the average activity of the 12 M units when reaching to one of the 8 targets, projected onto the jPCA plane. The signature of a rotational structure in these plots is that most trajectories circulate in a counterclockwise direction. Quantitatively, the first jPCA plane (out of six) captures (.42±.04, .42±.04, .46±.03, .45±.04, .47±.07) of the variance.

With this analysis we show that the quasi-oscillations observed after reach onset could arise from a sudden increase and subsequent decay of error in the loop. If this is the case, then their decay time should be correlated with the decay time of the error. Notice that this hypothesis is not very different from the interpretation in [87] (Supplemental Discussion, section 6.1), where a rotational movement in state space is observed as velocity rises and then falls.

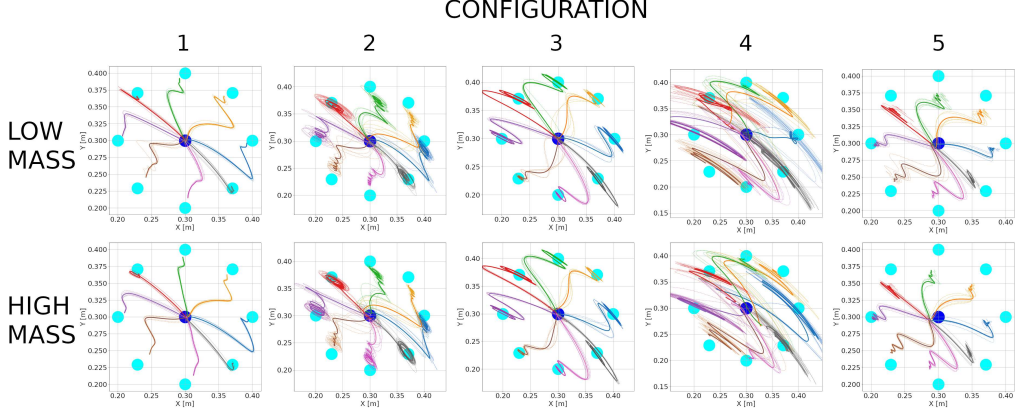


Figure 8: Hand trajectories with low mass (0.8 kg) and high mass (1.2 kg) for the 5 configurations.

2.5 The effect of changing the mass

Physical properties of the arm can change, not only as the arm grows, but also when tools or new environments come into play. As a quick test of whether the properties in this paper are robust to moderate changes, we changed the mass of the arm and forearm from 1 to 0.8 kg and ran one simulation for each of the 5 configurations.

With a lighter arm the average errors during center-out reaching were (2.5, 3.2, 3, 6.1, 2.9) cm. The biggest difference with previous values (section 2.3) came in configuration 4, which entered an oscillatory regime. One explanation is that reducing the mass is akin to increasing the gain, and this system was already at the verge of instability. We have not explored whether the synergistic configuration has a larger sensitivity to changes in the loop's gain.

In the same simulation, after the center-out reaching was completed, we once more modified the mass of the arm and forearm, from 0.8 to 1.2 kg, after which we began the center-out reaching again. This time the center-out reaching errors were (2.4, 3.3, 2.9, 5.6, 3.2) cm, very similar to those with the lighter arm.

The results of the paper still held after these manipulations. For all configurations, PD vectors could be predicted with a coefficient of determination between .74 and .92; All units in M were significantly tuned to direction; the main axis of the PD distribution ranged between 56 and 61 degrees, and the first jPCA plane captured between 33% and 58% of the variance.

A plot of the hand trajectories with altered mass in all configurations is shown in figure 8. Trajectories for configurations 2 and 4 are visibly more oscillatory. Interestingly, oscillations around the target did not entirely disappear after the mass was increased, at least for the period when the 48 reaches were made.

2.6 Spinal stimulation produces convergent direction fields

Due to the viscoelastic properties of the muscles, the mechanical system without active muscle contraction will have a fixed point with lowest potential energy at the arm's rest position. Limited amounts of muscle contraction shift the position of that fixed point. This led us to question whether this could produce convergent force fields, which as discussed before are candidate motor primitives, and have been found experimentally.

To simulate local stimulation of an isolated spinal cord we removed all neuronal populations except for those in C , and applied inputs to the individual pairs of CE, CI units projecting to the same motoneuron. Doing this for different starting positions of the hand, and recording its initial direction of motion, produces a *direction field*. A direction field (DF) maps each initial hand location to a vector pointing in the average direction of the force that initially moves the hand. We used two different spinal circuits C for this test. The first one (C_1) is common to configurations 1,2,3,5, and the second one (C_2) is the one used for configuration 4 (the "synergistic" configuration).

The first two panels of figure 9 show the result of stimulating individual E-I pairs in C , which will indeed produce DFs with different fixed points.

We found that these DFs add approximately linearly (Fig. 9D). More precisely, let $D(a + b)$ be the DF from stimulating spinal locations a and b simultaneously, and $\alpha_{a+b}(x, y)$ be the angle of $D(a + b)$ at hand coordinates (x, y) . Using similar definitions for $D(a), D(b), \alpha_a(x, y), \alpha_b(x, y)$, we say the DFs add linearly if

$$\alpha_{a+b}(x, y) = \alpha_a(x, y) + \alpha_b(x, y), \quad \forall (x, y).$$

We define the mean angle difference between $D(a + b)$ and $D(a) + D(b)$ as

$$\gamma_{a,b} = \sum_{x,y} \frac{\alpha_{a+b}(x, y) - (\alpha_a(x, y) + \alpha_b(x, y))}{N_s}, \quad (4)$$

where N_s is the number of (x, y) sample points. We found that when averaged over the 15 (C_1) or 144 (C_2) possible (a, b) pairs, the mean of $\gamma_{a,b}$ was 13.5 degrees for C_1 , and 19.8 degrees for C_2 .

Randomly choosing two possibly different pairs (a, b) and (c, d) for the stimulation locations leads to a mean angle difference of 37.6 (C_1) or 72.3 degrees (C_2) degrees between the fields $D(a + b)$ and $D(c) + D(d)$ fields. A bootstrap test showed that these angles are significantly larger ($p < 0.0001$) than in the previous case where $(a, b) = (c, d)$.

The resting field is defined as the DF when no units are stimulated. Removing the resting field from $D(a + b), D(a)$, and $D(b)$ does not alter these results.

Recent macaque forelimb experiments [52] show that the magnitude of the vectors in the $D(a + b)$ fields is larger than expected from $D(a) + D(b)$ (supra-linear summation). We found no evidence for this effect, suggesting that it depends on mechanisms beyond those present in our model.

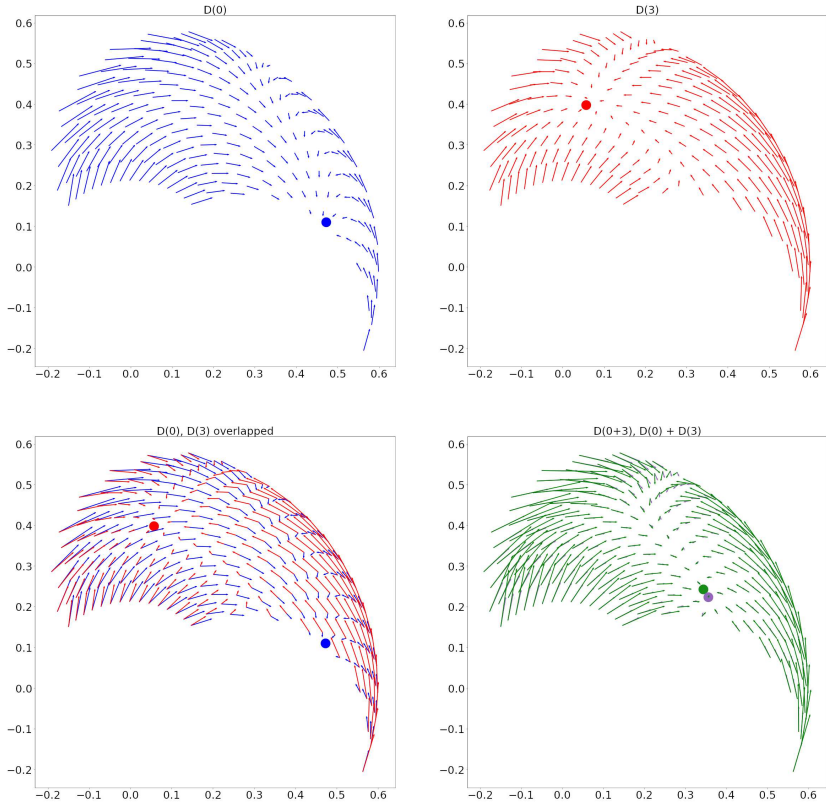


Figure 9: Two sample direction fields and their linear addition for circuit C_1 .
A: DF from stimulation of the interneurons for muscle 0 (biarticular biceps). The approximate location of the fixed point is shown with a blue dot. **B:** DF from stimulation of muscle 3 (biarticular triceps) interneurons. A red dot shows the fixed point. **C:** Panels A and B overlapped. **D:** In green, the DF from stimulating the interneurons for muscles 0 and 3 together. In purple, the sum of the DFs from panels A and B. Dots show the fixed points. The average angle between the green and purple vectors is 4 degrees.

3 Discussion

3.1 Summary of findings and predictions

We have presented a model of the long loop reflex with a main assumption: negative feedback configured with two differential Hebbian learning rules. One novel rule sets the loop’s input-output structure, and the other rule (input correlation) promotes stability. We showed that this model can make arm reaches by trying to perceive a given afferent pattern.

Our study made two central points:

1. Many experimental phenomena emerge from a feedback controller with minimally-complete musculoskeletal and neural models (emphasis is placed on the balance between excitation and inhibition).
2. Even if the feedback controller has multiple inputs and outputs, its input-output structure can be flexibly configured by a differential Hebbian learning rule, as long as errors are monotonic.

We presented five configurations of our model, each bringing a different argument to the table. Configuration 3, with no synaptic plasticity, illustrates point 1 above: feedback control is enough to bring forth the phenomena in the Results section. Configuration 1 (learning in the connections from M to C) presents the hypothesis that the spinal cord learns to adaptively configure this controller. Configurations 4 and 5 continue this hypothesis.

In configuration 5 the M units can receive multiple inputs from S_{PA} , suggesting that they could potentially learn to represent more abstract errors, as long as the monotonicity constraint is maintained. In addition to being more biological than configuration 1, configuration 5 has a larger drift in PD vectors (see Supplementary section 8), and provides a simple explanation why the activity in M units does not need to strongly correlate with the contraction of individual muscles. Configuration 4 shows that co-activation of multiple muscles by spinal cord neurons is compatible with our learning rules, opening the door for certain types of synergies.

Finally, configuration 2 shows that the input-output structure of the controller could in fact be a function of motor cortex; this would not disrupt our central claims. Configurations 1 and 2 should not be considered as incompatible hypotheses. Different elements performing overlapping functions are common in biological systems [88].

We list some properties of the model, and possible implications:

- Basic arm reaching happens through negative feedback, trying to perceive a target value set in cortex. Learning the input-output structure of the feedback controller may require spinal cord plasticity.
 - Cerebellar patients should not be able to adapt to tasks that require fast reactions, as negative feedback alone cannot compensate for delays in the system [89]. On the other hand, they should be able

to learn tasks that require remapping afferent inputs to movements. One example is [90], where cerebellar patients learned to move in a novel dynamic environment, but their movements were less precise than those of controls.

- The shape of reaches is dominated by mechanical and viscoelastic properties of the arm and muscles.
 - Unfamiliar viscous forces as in [90] should predictably alter the trajectory (Fig. 3) for cerebellar patients, who should not be able to adapt unless they move slowly and are explicitly compensating.
- Preferred Directions (PDs) in motor cortex happen because muscles need to contract more when reaching in certain directions.
 - The PD distribution should align with the directions where the muscles need to contract to reduce the error. These directions depend on which error S_{PA} is encoding. If the error is not related to reaching (e.g. related to haptic feedback), a different PD distribution may arise after overtraining.
 - Drift in the PD vectors comes from the ongoing adaptation, and it should not disrupt performance.
- Quasi-oscillations observed in motor cortex activity after the onset of movement reflect the decrease in the error signal.
 - The decay time of quasi-oscillations in motor cortex after movement onset will correlate with the error decay.
- Convergent force fields happen naturally in musculoskeletal systems when there is balance in the stimulation between agonists and antagonists. Linear addition of force fields is a result of forces/torques adding linearly.

Since our relatively simple model could reproduce all these phenomena, we believe it constitutes a good null hypothesis for all of them. But beyond explaining experimental observations, this model makes inroads into the hard problem of how the central nervous system (CNS) can generate effective control signals, recently dubbed the “supraspinal pattern formation” problem [77]. From our perspective, the CNS does not need to generate precise activation patterns for muscles and synergies; it needs to figure out which perceptions need to change. It is subcortical structures that learn the movement details. The key to make such a model work is the differential Hebbian learning framework in [11], which handles the final credit assignment problem.

We chose not to include a model of the cerebellum at this stage. Our model reflects the brain structure of an infant baby who can make clumsy reaching movements. At birth the cerebellum is incomplete and presumably not functional. It requires structured input from spinal cord and cortex to establish correct synaptic connections during postnatal development and will contribute to smooth reaching movements at a later age.

Encompassing function, learning, and experimental phenomena in a single simple model is a promising start towards a more integrated computational neuroscience. Moreover, predictive simple models have the potential to steer complex large-scale models so they can also achieve learning and functionality from scratch.

4 Methods

Simulations were run in the Draculab simulator [91]. All the parameters from the equations in this paper are presented in the Supplementary information (section 11). Parameters not shown can be obtained from Python dictionaries in the source code. This code can be downloaded from:

https://gitlab.com/sergio.verduzco/public_materials/-/tree/master/adaptive_plasticity

4.1 Unit equations

With the exception of the A and S_P populations, the activity u_i of any unit in figure 1 has dynamics:

$$\tau_u \dot{u}_i = \sigma(I) - u_i, \quad (5)$$

$$\sigma(I) = \frac{1}{1 + \exp(\beta(I - \eta))}, \quad (6)$$

where τ is a time constant, β is the slope of the sigmoidal function, η is its threshold, and $I = \sum_j \omega_{ij} u_j(t - \Delta t_j)$ is the sum of delayed inputs times their synaptic weights.

Units in the CE, CI populations had an additional noise term, which turned equation 5 into this Langevin equation:

$$du_i(t) = \frac{1}{\tau_u} (\sigma(I) - u_i(t)) + \varsigma dW(t), \quad (7)$$

where $W(t)$ is a Wiener process with unit variance, and ς is a parameter to control the noise amplitude. This equation was solved using the Euler-Maruyama method. All other unit equations were integrated using the forward Euler method. The equations for the plant and the muscles were integrated with SciPy's (<https://scipy.org/>) explicit Runge-Kutta 5(4) method.

Units in the A population use a rectified logarithm activation function, leading to these dynamics for their activity:

$$\tau_a \dot{a} = \log([1 + I - T]_+) - a, \quad (8)$$

where τ_a is a time constant, I is the scaled sum of inputs, T is a threshold, and $[x]_+ = \max(x, 0)$ is the "positive part" function.

4.2 Learning rules

The learning rule for the connections from M to CE, CI units was first described in [11]. It has an equation:

$$\dot{\omega}_{ij}(t) = -\left(\ddot{e}_j(t) - \langle \ddot{e}(t) \rangle\right)\left(\dot{c}_i(t - \Delta t) - \langle \dot{c}(t - \Delta t) \rangle\right). \quad (9)$$

In this equation, $e_j(t)$ represents the activity of the j -th unit in M at time t , and $\ddot{e}_j(t)$ is its second derivative. Angle brackets denote averages, so that $\langle \ddot{e} \rangle \equiv \frac{1}{N_M} \sum_k \ddot{e}_k$, where N_M is the number of M units. $\dot{c}_i(t)$ is the derivative of the activity for the postsynaptic unit, and Δt is a time delay ensuring that the rule captures the proper temporal causality. The supplementary discussion (section 6.2) elaborates on how such a learning rule could be present in the spinal cord.

The learning rule in 9 was also fitted with soft weight-bounding to prevent connections from changing sign, and multiplicative normalization was used to control the magnitude of the weights by ensuring two requirements: (1) all weights from projections of the same M unit should add to w_{sa} , (2) all weights ending at the same C unit should add to w_{sb} . With this, the learning rule adopted the form:

$$\dot{\omega}_{ij} = -\alpha \omega_{ij} \left(-\Delta + \lambda [(0.5(\zeta_{sa} + \zeta_{sb}) - 1)] \right), \quad (10)$$

In this equation α is a constant learning rate, Δ is the right-hand side expression of equation 9, and λ is a scalar parameter. The value ζ_{sa} is w_{sa} divided by the sum of outgoing weights from the j -th M unit, and ζ_{sb} is w_{sb} divided by the sum of incoming M weights on c_i . This type of normalization is meant to reflect the competition for resources among synapses, both at the presynaptic and postsynaptic level.

The synapses in the connections from A to M and from A to C used the input correlation rule [66]:

$$\dot{w} = \alpha_{IC} w I_A \dot{I}_{PA}, \quad (11)$$

where I_A is the scaled sum of inputs from the A population, α_{IC} is the learning rate, I_{PA} is the scaled sum of inputs from S_{PA} or M , and \dot{I}_{PA} is its derivative. Unlike the original input correlation rule, this rule uses soft weight bounding to avoid weights changing signs. Moreover, the sum of the weights was kept close to a ω_s value. In practice this meant dividing the each individual w value by the sum of weights from A -to- M connections, and multiplying times ω_s at each update. In addition, weight clipping was used to keep individual weights below a value ω_{max} .

4.3 Exploratory mechanism

Without any additional mechanisms the model risked getting stuck in a fixed arm position before it could learn. We included two mechanisms to permit

exploration in the system. The first mechanism consists of intrinsic noise in the *CE* and *CI* interneurons, which causes low-amplitude oscillations in the arm. We have observed that intrinsic oscillations in the *CE*, *CI* units are also effective to allow learning (data not shown), but the option of intrinsic noise permits the use of simple sigmoidal units in *C*, and contributes to the discussion regarding the role of noise in neural computation.

The second mechanism for exploration consists of an additional unit, called *ACT*. This unit acted similarly to a leaky integrator of the total activity in S_{PA} , reflecting the total error. If the leaky integral of the S_{PA} activity crossed a threshold, then *ACT* would send a signal to all the *CE* and *CI* units, causing adaptation. The adaptation consisted of an inhibitory current that grew depending on the accumulated previous activity.

To model this, *CE* and *CI* units received an extra input I_{adapt} . When the input from the *ACT* unit was larger than 0.8, and $I_{adapt} < 0.2$, the value of I_{adapt} would be set to $(u_i^{slow})^2$. This is the square of a low-passed filtered version of u_i . More explicitly,

$$\tau_{slow} \dot{u}_i^{slow} = u_i - u_i^{slow}. \quad (12)$$

If the input from *ACT* was smaller than 0.8, or I_{adapt} became larger than 0.2, then I_{adapt} would decay towards zero:

$$\tau_{slow} \dot{I}_{adapt} = -I_{adapt}. \quad (13)$$

With this mechanism, if the arm got stuck then error would accumulate, leading to adaptation in the spinal interneurons. This would cause the most active interneurons to receive the most inhibition, shifting the “dominant” activities, and producing larger-amplitude exploratory oscillations.

When a new target is presented, *ACT* must reset its own activity back to a low value. Given our requirement to fully implement the controller using neural elements, we needed a way to detect changes in S_P . A unit denominated *CHG* can detect these changes using synapses that react to the derivative of the activity in S_P units. *CHG* was connected to *ACT* in order to reset its activity.

More precisely, when inputs from *CHG* were larger than 0.1, the activity of *ACT* had dynamics:

$$\dot{a}(t) = -40a(t). \quad (14)$$

Otherwise it had these dynamics:

$$\dot{a}(t) = a(t)(\sigma(I) - \theta_{ACT}), \text{ if } \sigma(I) < \theta_{ACT}, \quad (15)$$

$$\tau_{ACT} \dot{a}(t) = (\sigma(I) - \theta_{ACT})[1 - a(t) + \gamma \dot{\sigma}(I)], \text{ otherwise.} \quad (16)$$

As before, $\sigma(\cdot)$ is a sigmoidal function, and I is the scaled sum of inputs other than *CHG*. When $\sigma(I)$ is smaller than a threshold θ_{ACT} the value of a actually decreases, as this error is deemed small enough. When $\sigma(I) > \theta_{ACT}$ the activity increases, but the rate of increase is modulated by a rate of increase $\dot{\sigma}(I) \equiv \sigma(I) - \sigma(\tilde{I})$, where \tilde{I} is a low-pass filtered version of I . γ is a constant parameter.

CHG was a standard sigmoidal unit receiving inputs from S_P , with each synaptic weight obeying this equation:

$$\omega_j(t) = \alpha |\dot{s}_j(t)| - \omega_j(t), \quad (17)$$

where s_j represents the synapse's presynaptic input.

4.4 Plant, muscles, afferents

The planar arm was modeled as a compound double pendulum, where both the arm and forearm were cylinders with 1 kg. of mass. No gravity was present, and a moderate amount of viscous friction was added at each joint ($3 \frac{N \cdot m}{rad}$). The derivation and validation of the double pendulum's equations can be consulted in a Jupyter notebook included with Draculab's source code (in the `tests` folder).

The muscles used a standard Hill-type model, as described in [7], Pg. 99. The muscle's tension T obeys:

$$\dot{T} = \frac{K_{SE}}{b} \left[g \cdot I + K_{PE} \Delta x + b \dot{x} - \left(1 + \frac{K_{PE}}{K_{SE}} \right) T \right], \quad (18)$$

where I is the input, g an input gain, K_{PE} the parallel elasticity constant, K_{SE} the series elasticity constant, b is the damping constant for the parallel element, x is the length of the muscle, and $\Delta x = x - x_1^* - x_2^*$. In here, x_1^* is the resting length of the series element, whereas x_2^* is the resting length of the parallel element. All resting lengths were calculated from the steady state when the hand was located at coordinates (0.3, 0.3).

We created a model of the Ia and II afferents using simple structural elements. This model includes, for each muscle one dynamic nuclear bag fiber, and one static bag fiber. Both of these fibers use the same tension equation as the muscle, but with different parameters. For the static bag fiber:

$$\dot{T}^s = \frac{K_{SE}^s}{b^s} \left[K_{PE}^s \Delta x + b^s \dot{x} - \left(1 + \frac{K_{PE}^s}{K_{SE}^s} \right) T^s \right]. \quad (19)$$

The dynamic bag fiber uses the same equation, with the s superscript replaced by d . No inputs were applied to the static or dynamic bag fibers, so they were removed from these equations. The rest lengths of the static and dynamic bag fibers were those of their corresponding muscles times factors l_0^s, l_0^d , respectively.

The Ia afferent output is proportional to a linear combination of the lengths for the serial elements in both dynamic and static bag fibers. The II output has two components, one proportional to the length of the serial element, and one approximately proportional to the length of the parallel element, both in the static bag fiber. In practice this was implemented through the following equations:

$$I_a = g_{I_a} \left[\left(\frac{f_s^{I_a}}{K_{SE}^s} \right) T^s + \left(\frac{1 - f_s^{I_a}}{K_{SE}^d} \right) T^d \right], \quad (20)$$

$$II = g_{II} \left[\left(\frac{f_s^{II}}{K_{SE}^s} \right) T^s + \left(\frac{1 - f_s^{II}}{K_{PE}^s} \right) (T^s - b^s \dot{x}) \right]. \quad (21)$$

In here, g_{I_a} and g_{II} are gain factors. $f_s^{I_a}$ and f_s^{II} are constants determining the fraction of I_a and II output that comes from the serial element.

The model of the Golgi tendon organ producing the Ib outputs was taken from [92]. First, a rectified tension was obtained as:

$$r = g_{I_b} \log(T^+/T_0 + 1). \quad (22)$$

g_{I_b} is a gain factor, T_0 is a constant that can further alter the slope of the tension, and $T^+ = \max(T, 0)$ is the tension, half-rectified. The I_b afferent output followed dynamics:

$$\tau_{I_b} \dot{I}_b = r - I_b. \quad (23)$$

4.5 Static connections

In all cases the connections to S_A used one-to-one connectivity with the A units driven by the II afferents, whereas connections from A to M and C used all-to-all projections from the units driven by the Ia and Ib afferents. Projections from S_A to S_{PA} used one-to-one excitatory connections to the first 6 units, and inhibitory projections to the next 6 units. Projections from S_P to S_{PA} used the opposite sign from this.

In configurations 1-4 the connections from S_{PA} to M were one-to-one, so the j -th unit in S_{PA} only sent a projection to unit j in M . In configuration 5 each M unit received a linear combination of S_{PA} inputs. The connectivity matrix for this case was based on the following 6-dimensional orthogonal matrix:

$$R = \begin{bmatrix} 1 & 1 & 1 & 1 & 1 & 1 \\ 1 & 1 & 1 & -1 & -1 & -1 \\ 1 & -2 & 1 & -1 & 2 & -1 \\ -1 & -1 & 2 & 2 & -1 & -1 \\ -1 & 1 & 0 & 0 & 1 & -1 \\ -1 & 0 & 1 & -1 & 0 & 1 \end{bmatrix}. \quad (24)$$

The rows of this matrix form an orthogonal basis in \mathbb{R}^6 , and normalizing each row we obtain a matrix R^* whose rows form an orthonormal basis. Connections from the 12 S_{PA} units to the 12 M units used this 12×12 matrix:

$$\begin{bmatrix} R^* & -R^* \\ -R^* & R^* \end{bmatrix}. \quad (25)$$

In configuration 4 the units of activation consisted of pairs of muscles. As illustrated in figure S5, from the set of 6 muscles there are 15 combinations of 2 muscles, but 3 of them consist of antagonist pairs. Removing these we are left with 12 pairs of muscles, and for each muscle pair we had a Wilson-Cowan-like CE, CI pair sending projections to both of them. Furthermore, for each pair of

muscles, there is another pair that contains both their antagonists, and we can use this fact to generalize the concept of antagonists when interneurons project to several motoneurons. The *CE* units sent projections to the *CI* units of their antagonists. This organization allowed us to maintain the balance between excitation and inhibition in the network, along with the connectivity motifs used previously.

All the connections in configuration 3 are static. We explain how we adjusted the synaptic weights of the otherwise plastic connections. To understand the projections from *M* to *C* and to the alpha motoneurons it is useful to remember that each *CE*, *CI*, α trio is associated with one muscle, and the *M* units also control the error of a single muscle. This error indicates that the muscle is longer than desired. Thus, the *M* unit associated with muscle *i* sent excitatory projections to the *CE* and α units associated with muscle *i*, and to the *CI* units of the antagonists of *i*. Additionally, weaker projections were sent to the *CE*, α units of muscle *i*'s agonists. Notice that only excitatory connections were used.

The reverse logic was used to set the connections from *A* to *C* and *M*. If muscle *i* is tensing or elongating, this can predict an increase in the error for its antagonists, which is the kind of signal that the input correlation rule is meant to detect. Therefore, the *Ib* afferent (signaling tension) of muscle *i* sent an excitatory signal to the *CI* unit associated with muscle *i*, and to the *CE*, α units associated with *i*'s antagonists. Moreover, this *Ib* afferent also sent an excitatory projection to the dual of the *M* unit associated with muscle *i*. Connections from *Ia* afferents (roughly signaling elongation speed) followed the same pattern, but with slightly smaller connection strengths.

4.6 Rotational dynamics

We explain the method to project the activity of *M* onto the jPCA plane. For all units in *M* we considered the activity during a 0.5 seconds sample beginning 50 milliseconds after the target onset. Unlike [41], we did not apply PCA preprocessing, since we only have 12 units in *M*. Let $m_{i,j,k,t}$ be the activity at time *t* of the unit *i* in *M*, when reaching at target *j* for the *k*-th repetition. By $m_{i,j,\langle k \rangle,t}$ we denote the average over all repeated reaches to the same target, and by $m_{i,\langle j \rangle,\langle k \rangle,t}$ we indicate averaging over both targets and repetitions. The normalized average trace per condition is defined as: $m_{i,j}(t) \equiv m_{i,j,\langle k \rangle,t} - m_{i,\langle j \rangle,\langle k \rangle,t}$. Let *I* stand for the number of units in *M*, *T* for the number of time points, and *J* for the number of targets. Following [41], we unroll the set of $m_{i,j}(t)$ values into a matrix $X \in R^{JT \times I}$, so we may represent the data through a matrix *M* that provides the least-squares solution to the problem $\dot{X} = XM$. This solution comes from the equation $\hat{M} = (X^T X)^{-1} X^T \dot{X}$. Furthermore, this matrix can be decomposed into symmetric and anti-symmetric components $M_{symm} = (\hat{M} + \hat{M}^T)/2$, $M_{skew} = (\hat{M} - \hat{M}^T)/2$. The jPCA plane comes from the complex conjugate eigenvalues of M_{skew} .

In practice, our source code follows the detailed explanation provided in the Supplementary Information of [41], which reformulates this matrix problem as a vector problem.

4.7 Parameter search

We kept all parameter values in a range where they still made biological sense. Parameter values that were not constrained by biological data were adjusted using a genetic algorithm, and particle swarm optimization (PSO). We used a separate optimization run for each one of the configurations, consisting of roughly 30 iterations of the genetic and PSO algorithms, with populations sizes of 90 and 45 individuals respectively. After this we adjusted the gain of the control loop by increasing or decreasing the slope of the sigmoidal units in the M and S_A populations. This is further described in the Supplementary Information (section 9).

The parameters used can affect the results in the paper. We chose parameters that minimized either the error during the second half of the learning phase, or the error during center-out reaching. Both of these measures are agnostic to the other results.

4.8 Preferred direction vectors

Next we describe how PD vectors were obtained for the M units.

Let m_{jk} denote the firing rate of the j -th M unit when reaching for the k -th target, averaged over 4 seconds, and across reaches to the same target. We created a function $h_j : \mathbb{R}^2 \rightarrow \mathbb{R}$ that mapped the X, Y coordinates of each target to its corresponding m_{jk} value, but in the domain of h_j the coordinates were shifted so the center location was at the origin.

Next we approximated h_j with a plane, using the least squares method, and obtained a unit vector u_j normal to that plane, starting at the intersection of the z -axis and the plane, and pointing towards the XY plane. The PD vector was defined as the projection of u_j on the XY plane.

In order to predict the PD vectors, we first obtained for each muscle the “direction of maximum contraction,” verbally described in panel B of figure 5. More formally, let l_{ik} denote the length of the i -th muscle when the hand is at target k , and let l_i^0 denote its length when the hand is at the center location. With \bar{r}_k we denote the unit vector with base at the center location, pointing in the direction of the k -th target. The direction of maximum length change for the i -th muscle comes from the following vector sum:

$$\bar{v}_i = \sum_{k=1}^8 \left[\frac{l_i^0 - l_{ik}}{l_i^0} \right]_+ \bar{r}_k, \quad (26)$$

where $[x]_+ = \max(x, 0)$.

For the j -th unit in M , its predicted PD vector comes from a linear combination of the \bar{v}_i vectors. Let the input to this unit be $\sum_i w_{ji} e_i$, where e_i is the output of the i -th SPF unit (representing the error in the i -th muscle). The predicted PD vector is:

$$\bar{d}_j = \sum_{i=0}^5 w_{ji} \bar{v}_i \quad (27)$$

To obtain the main axis of the PD distribution, the i -th PD vector was obtained in the polar form (r_i, θ_i) , with $\theta \in (-\pi, \pi]$. We reflected vectors in the lower half using the rule: $\theta_i^* = \theta_i + \pi$ if $\theta_i < 0$, $\theta_i^* = \theta_i$ otherwise. The angle of the main axis was the angle of the average PD vector using these modified angles: $\theta_{main} = \arctan\left(\frac{\sum_i r_i \sin \theta_i^*}{\sum_i r_i \cos \theta_i^*}\right)$.

4.9 Statistical tests

To find whether M units were significantly tuned to the reach direction we used a bootstrap procedure. For each unit we obtained the length of its PD vector 10,000 times when the identity of the target for each reach was randomly shuffled. We considered there was significant tuning when the length of the true PD vector was longer than 99.9% of these random samples.

To obtain the coefficient of determination for the predicted PD angles, let θ_{true}^j denote the angle of the true PD for the j -th M unit, and θ_{pred}^j be the angle of its predicted PD. We obtained residuals for the angles as $\epsilon_j = \theta_{true}^j - \theta_{pred}^j$, where this difference is actually the angle of the smallest rotation that turns one angle into the other. Each residual was then scaled by the norm of its corresponding PD vector, to account for the fact that these were not homogeneous. Denoting these scaled residuals as ϵ_j^* the residual sum of squares is $SS_{res} = \sum_j (\epsilon_j^*)^2$. The total sum of squares was: $SS_{tot} = \sum_j (\theta_{true}^j - \bar{\theta}_{true})^2$, where $\bar{\theta}_{true}$ is the mean of the θ_{true}^j angles. The coefficient of determination comes from the usual formula $R^2 = 1 - \frac{SS_{res}}{SS_{tot}}$.

To assess bimodality of the PD distribution we used a version of the Rayleigh statistic adapted to look for bimodal distributions where the two modes are oriented at 180 degrees from each other, introduced in [83]. This test consists of finding an modified Rayleigh r statistic defined as:

$$r = \frac{1}{N} \left(\left(\sum_{i=1}^N \cos(2\phi_i) \right)^2 + \left(\sum_{i=1}^N \sin(2\phi_i) \right)^2 \right), \quad (28)$$

where the ϕ_i angles are the angles for the PDs. A bootstrap procedure is then used, where this r statistic is produced 100,000 times by sampling from the uniform distribution on the $(0, \pi)$ interval. The PD distribution was deemed significantly bimodal if its r value was larger than 99.9% of the random r values.

We used a bootstrap test to find whether there was statistical significance to the linear addition of direction fields. To make this independent of the individual pair of locations stimulated, we obtained the direction fields for all 15 possible pairs of locations, and for each pair calculated the mean angle difference between $D(a+b)$ and $D(a) + D(b)$ as described in the main text. We next obtained the mean of these 15 average angle deviations, to obtain a global average angle deviation γ_{global} .

We then repeated this procedure 400 times when the identities of the stimulation sites a, b were shuffled, to obtain 400 global average angle deviations

γ_{global}^j . We declared statistical significance if γ_{global} was smaller than 99% of the γ_{global}^j values.

5 Acknowledgements

The authors wish to thank Prof. Kenji Doya for helping revise early versions of this manuscript.

References

- [1] Kaas, J. H. & Collins, C. E. *The Primate Visual System* (CRC Press, 2003). Google-Books-ID: rRu38JwnZXoC.
- [2] Ballard, D. H. & Zhang, R. The Hierarchical Evolution in Human Vision Modeling. *Topics in Cognitive Science* **13**, 309–328 (2021). URL <https://onlinelibrary.wiley.com/doi/abs/10.1111/tops.12527>. eprint: <https://onlinelibrary.wiley.com/doi/pdf/10.1111/tops.12527>.
- [3] Chersi, F. & Burgess, N. The Cognitive Architecture of Spatial Navigation: Hippocampal and Striatal Contributions. *Neuron* **88**, 64–77 (2015). URL <https://www.sciencedirect.com/science/article/pii/S0896627315007783>.
- [4] Moser, E. I., Moser, M.-B. & McNaughton, B. L. Spatial representation in the hippocampal formation: a history. *Nature Neuroscience* **20**, 1448–1464 (2017). URL <https://www.nature.com/articles/nn.4653>. Bandiera_abtest: a Cg_type: Nature Research Journals Number: 11 Primary_atype: Comments & Opinion Publisher: Nature Publishing Group Subject_term: Hippocampus;Spatial memory Subject_term_id: hippocampus;spatial-memory.
- [5] Eccles, J. C. Physiology of Motor Control in Man. *Stereotactic and Functional Neurosurgery* **44**, 5–15 (1981). URL <https://www.karger.com/Article/FullText/102178>. Publisher: Karger Publishers.
- [6] Loeb, G. E. & Tsianos, G. A. Major remaining gaps in models of sensorimotor systems. *Frontiers in Computational Neuroscience* **9** (2015). URL <https://www.frontiersin.org/articles/10.3389/fncom.2015.00070/full>. Publisher: Frontiers.
- [7] Shadmehr, R. & Wise, S. P. *The Computational Neurobiology of Reaching and Pointing: A Foundation for Motor Learning* (MIT Press, 2005). Google-Books-ID: fKeImql1s.sC.
- [8] Arber, S. & Costa, R. M. Connecting neuronal circuits for movement. *Science* **360**, 1403–1404 (2018). URL

<https://www.science.org/lookup/doi/10.1126/science.aat5994>.

Publisher: American Association for the Advancement of Science.

- [9] Tanaka, Y. H. *et al.* Thalamocortical Axonal Activity in Motor Cortex Exhibits Layer-Specific Dynamics during Motor Learning. *Neuron* **100**, 244–258.e12 (2018). URL <https://www.sciencedirect.com/science/article/pii/S0896627318306895>.
- [10] Hadders-Algra, M. Early human motor development: From variation to the ability to vary and adapt. *Neuroscience & Biobehavioral Reviews* **90**, 411–427 (2018). URL <https://www.sciencedirect.com/science/article/pii/S0149763418300538>.
- [11] Verduzco-Flores, S., Dorrell, W. & De Schutter, E. A differential Hebbian framework for biologically-plausible motor control. *Neural Networks* **150**, 237–258 (2022). URL <https://www.sciencedirect.com/science/article/pii/S0893608022000727>.
- [12] Woods, S. C. & Ramsay, D. S. Homeostasis: Beyond Curt Richter. *Appetite* **49**, 388–398 (2007). URL <https://www.sciencedirect.com/science/article/pii/S019566630700270X>.
- [13] Bizzi, E., Tresch, M. C., Saltiel, P. & d'Avella, A. New perspectives on spinal motor systems. *Nature Reviews Neuroscience* **1**, 101–108 (2000). URL <https://www.nature.com/articles/35039000>.
- [14] Lemon, R. N. Descending Pathways in Motor Control. *Annual Review of Neuroscience* **31**, 195–218 (2008). URL <https://www.annualreviews.org/doi/10.1146/annurev.neuro.31.060407.125547>.
- [15] Arber, S. Motor Circuits in Action: Specification, Connectivity, and Function. *Neuron* **74**, 975–989 (2012). URL <https://www.sciencedirect.com/science/article/pii/S0896627312004771>.
- [16] Asante, C. O. & Martin, J. H. Differential Joint-Specific Corticospinal Tract Projections within the Cervical Enlargement. *PLOS ONE* **8**, e74454 (2013). URL <https://journals.plos.org/plosone/article?id=10.1371/journal.pone.0074454>.
- [17] Alstermark, B. & Isa, T. Circuits for Skilled Reaching and Grasping. *Annual Review of Neuroscience* **35**, 559–578 (2012). URL <https://doi.org/10.1146/annurev-neuro-062111-150527>.
- [18] Jankowska, E. Spinal Interneurons. In Pfaff, D. W. (ed.) *Neuroscience in the 21st Century: From Basic to Clinical*, 1063–1099 (Springer, New York, NY, 2013). URL https://doi.org/10.1007/978-1-4614-1997-6_34.
- [19] Wang, X. *et al.* Deconstruction of Corticospinal Circuits for Goal-Directed Motor Skills. *Cell* **171**, 440–455.e14 (2017). URL <https://www.sciencedirect.com/science/article/pii/S009286741730939X>.

[20] Ueno, M. *et al.* Corticospinal Circuits from the Sensory and Motor Cortices Differentially Regulate Skilled Movements through Distinct Spinal Interneurons. *Cell Reports* **23**, 1286–1300.e7 (2018). URL <http://www.sciencedirect.com/science/article/pii/S2211124718305254>.

[21] Wolpaw, J. R., Kieffer, V. A., Seegal, R. F., Braitman, D. J. & Sanders, M. G. Adaptive plasticity in the spinal stretch reflex. *Brain Research* **267**, 196–200 (1983). URL <https://www.sciencedirect.com/science/article/pii/0006899383910594>.

[22] Grau, J. W. Learning from the spinal cord: How the study of spinal cord plasticity informs our view of learning. *Neurobiology of Learning and Memory* **108**, 155–171 (2014). URL <https://www.sciencedirect.com/science/article/pii/S1074742713001445>.

[23] Meyer-Lohmann, J., Christakos, C. N. & Wolf, H. Dominance of the short-latency component in perturbation induced electromyographic responses of long-trained monkeys. *Experimental Brain Research* **64**, 393–399 (1986). URL <https://doi.org/10.1007/BF00340475>.

[24] Wolpaw, J. R. The complex structure of a simple memory. *Trends in Neurosciences* **20**, 588–594 (1997). URL <http://www.sciencedirect.com/science/article/pii/S0166223697011338>.

[25] Norton, J. J. & Wolpaw, J. R. Acquisition, maintenance, and therapeutic use of a simple motor skill. *Current Opinion in Behavioral Sciences* **20**, 138–144 (2018). URL <http://www.sciencedirect.com/science/article/pii/S235215461730219X>.

[26] Georgopoulos, A., Kalaska, J., Caminiti, R. & Massey, J. On the relations between the direction of two-dimensional arm movements and cell discharge in primate motor cortex. *The Journal of Neuroscience* **2**, 1527–1537 (1982). URL <https://www.ncbi.nlm.nih.gov/pmc/articles/PMC6564361/>.

[27] Georgopoulos, A. P., Schwartz, A. B. & Kettner, R. E. Neuronal population coding of movement direction. *Science* **233**, 1416–1419 (1986). URL <https://science.sciencemag.org/content/233/4771/1416>. Publisher: American Association for the Advancement of Science Section: Reports.

[28] Kakei, S., Hoffman, D. S. & Strick, P. L. Muscle and Movement Representations in the Primary Motor Cortex. *Science* (1999). URL <https://www.science.org/doi/abs/10.1126/science.285.5436.2136>. Publisher: American Association for the Advancement of Science.

[29] Truccolo, W., Friehs, G. M., Donoghue, J. P. & Hochberg, L. R. Primary Motor Cortex Tuning to Intended Movement Kinematics in Humans with Tetraplegia. *Journal of Neuroscience* **28**, 1163–1178 (2008). URL

<https://www.jneurosci.org/content/28/5/1163>. Publisher: Society for Neuroscience Section: Articles.

- [30] Kalaska, J. F. From intention to action: motor cortex and the control of reaching movements. *Advances in Experimental Medicine and Biology* **629**, 139–178 (2009).
- [31] Georgopoulos, A. P. & Stefanis, C. N. Local shaping of function in the motor cortex: Motor contrast, directional tuning. *Brain Research Reviews* **55**, 383–389 (2007). URL <https://www.sciencedirect.com/science/article/pii/S0165017307000720>.
- [32] Harrison, T. C. & Murphy, T. H. Towards a circuit mechanism for movement tuning in motor cortex. *Frontiers in Neural Circuits* **6** (2013). URL <https://www.frontiersin.org/articles/10.3389/fncir.2012.00127/full>. Publisher: Frontiers.
- [33] Tanaka, H. Modeling the motor cortex: Optimality, recurrent neural networks, and spatial dynamics. *Neuroscience Research* **104**, 64–71 (2016). URL <https://www.sciencedirect.com/science/article/pii/S0168010215002631>.
- [34] Morrow, M. M. & Miller, L. E. Prediction of Muscle Activity by Populations of Sequentially Recorded Primary Motor Cortex Neurons. *Journal of Neurophysiology* **89**, 2279–2288 (2003). URL <https://journals.physiology.org/doi/full/10.1152/jn.00632.2002>. Publisher: American Physiological Society.
- [35] Todorov, E. Direct cortical control of muscle activation in voluntary arm movements: a model. *Nature Neuroscience* **3**, 391–398 (2000). URL https://www.nature.com/articles/nn0400_391.
- [36] Scott, S. H., Gribble, P. L., Graham, K. M. & Cabel, D. W. Dissociation between hand motion and population vectors from neural activity in motor cortex. *Nature* **413**, 161–165 (2001). URL <https://www.nature.com/articles/35093102>.
- [37] Rokni, U., Richardson, A. G., Bizzi, E. & Seung, H. S. Motor Learning with Unstable NeuralRepresentations. *Neuron* **54**, 653–666 (2007). URL <https://www.sciencedirect.com/science/article/pii/S0896627307003339>.
- [38] Padoa-Schioppa, C., Li, C.-S. R. & Bizzi, E. Neuronal Activity in the Supplementary Motor Area of Monkeys Adapting to a New Dynamic Environment. *Journal of Neurophysiology* **91**, 449–473 (2004). URL <https://journals.physiology.org/doi/full/10.1152/jn.00876.2002>. Publisher: American Physiological Society.
- [39] Shenoy, K. V., Sahani, M. & Churchland, M. M. Cortical Control of Arm Movements: A Dynamical Systems Perspective. *Annual Review of Neuroscience* **36**, 337–359 (2013). URL <http://www.annualreviews.org/doi/10.1146/annurev-neuro-062111-150509>.

[40] Sussillo, D., Churchland, M. M., Kaufman, M. T. & Shenoy, K. V. A neural network that finds a naturalistic solution for the production of muscle activity. *Nature Neuroscience* **18**, 1025–1033 (2015). URL <https://www.nature.com/articles/nn.4042>.

[41] Churchland, M. *et al.* Neural population dynamics during reaching. *Nature* **487**, 51–56 (2012). URL <https://www.ncbi.nlm.nih.gov/pmc/articles/PMC3393826/>.

[42] Schöner, G., Tekülve, J. & Zibner, S. Reaching for objects: a neural process account in a developmental perspective. In *Reach-to-Grasp Behavior*, 281–318 (Routledge, 2018).

[43] Valero-Cuevas, F. J. A mathematical approach to the mechanical capabilities of limbs and fingers. *Advances in Experimental Medicine and Biology* **629**, 619–633 (2009).

[44] Keener, J. P. *Principles Of Applied Mathematics: Transformation And Approximation* (Avalon Publishing, 1995). Google-Books-ID: 5nlQAAAA-MAAJ.

[45] Giszter, S. F. Motor primitivesnew data and future questions. *Current Opinion in Neurobiology* **33**, 156–165 (2015). URL <http://www.sciencedirect.com/science/article/pii/S095943881500077X>.

[46] Mussa-Ivaldi, F. A. & Bizzi, E. Motor Learning through the Combination of Primitives. *Philosophical Transactions: Biological Sciences* **355**, 1755–1769 (2000). URL <https://www.jstor.org/stable/3066920>. Publisher: The Royal Society.

[47] Bizzi, E., Mussa-Ivaldi, F. A. & Giszter, S. Computations underlying the execution of movement: a biological perspective. *Science* **253**, 287–291 (1991). URL <https://science.sciencemag.org/content/253/5017/287>. Publisher: American Association for the Advancement of Science Section: Articles.

[48] Kelso, J. A. S. Synergies: Atoms of Brain and Behavior. In Sternad, D. (ed.) *Progress in Motor Control: A Multidisciplinary Perspective*, Advances in Experimental Medicine and Biology, 83–91 (Springer US, Boston, MA, 2009). URL https://doi.org/10.1007/978-0-387-77064-2_5.

[49] Bruton, M. & ODwyer, N. Synergies in coordination: a comprehensive overview of neural, computational, and behavioral approaches. *Journal of Neurophysiology* **120**, 2761–2774 (2018). URL <https://journals.physiology.org/doi/full/10.1152/jn.00052.2018>. Publisher: American Physiological Society.

[50] Giszter, S. F., Mussa-Ivaldi, F. A. & Bizzi, E. Convergent force fields organized in the frog's spinal cord. *Journal of Neuroscience* **13**, 467–491 (1993). URL <https://www.jneurosci.org/content/13/2/467>. Publisher: Society for Neuroscience Section: Articles.

[51] Mussa-Ivaldi, F. A., Giszter, S. F. & Bizzi, E. Linear combinations of primitives in vertebrate motor control. *Proceedings of the National Academy of Sciences* **91**, 7534–7538 (1994). URL <https://www.pnas.org/content/91/16/7534>. Publisher: National Academy of Sciences Section: Research Article.

[52] Yaron, A., Kowalski, D., Yaguchi, H., Takei, T. & Seki, K. Forelimb force direction and magnitude independently controlled by spinal modules in the macaque. *Proceedings of the National Academy of Sciences* **117**, 27655–27666 (2020). URL <https://www.pnas.org/doi/full/10.1073/pnas.1919253117>. Publisher: Proceedings of the National Academy of Sciences.

[53] Tresch, M. C. & Jarc, A. The case for and against muscle synergies. *Current Opinion in Neurobiology* **19**, 601–607 (2009). URL <https://www.sciencedirect.com/science/article/pii/S095943880900124X>.

[54] de Rugy, A., Loeb, G. & Carroll, T. Are muscle synergies useful for neural control? *Frontiers in Computational Neuroscience* **0** (2013). URL <https://www.frontiersin.org/articles/10.3389/fncom.2013.00019/full>. Publisher: Frontiers.

[55] Bizzi, E. & Cheung, V. C. The neural origin of muscle synergies. *Frontiers in Computational Neuroscience* **7** (2013). URL <https://www.frontiersin.org/articles/10.3389/fncom.2013.00051/full>. Publisher: Frontiers.

[56] Levine, A. J. *et al.* Identification of a cellular node for motor control pathways. *Nature neuroscience* **17**, 586–593 (2014). URL <https://www.ncbi.nlm.nih.gov/pmc/articles/PMC4569558/>.

[57] Takei, T., Confais, J., Tomatsu, S., Oya, T. & Seki, K. Neural basis for hand muscle synergies in the primate spinal cord. *Proceedings of the National Academy of Sciences* **114**, 8643–8648 (2017). URL <https://www.pnas.org/content/114/32/8643>. Publisher: National Academy of Sciences Section: Biological Sciences.

[58] Pulvermiller, F., Tomasello, R., Henningsen-Schomers, M. R. & Wennekers, T. Biological constraints on neural network models of cognitive function. *Nature Reviews Neuroscience* 1–15 (2021). URL <https://www.nature.com/articles/s41583-021-00473-5>. Bandiera_abtest: a Cg-type: Nature Research Journals Primary_atype:

Reviews Publisher: Nature Publishing Group Subject_term: Cognitive neuroscience;Human behaviour;Network models Subject_term_id: cognitive-neuroscience;human-behaviour;network-models.

- [59] O'Reilly, R. C. Six principles for biologically based computational models of cortical cognition. *Trends in Cognitive Sciences* **2**, 455–462 (1998). URL <http://www.sciencedirect.com/science/article/pii/S1364661398012418>.
- [60] Richards, B. A. *et al.* A deep learning framework for neuroscience. *Nature Neuroscience* **22**, 1761–1770 (2019). URL <https://www.nature.com/articles/s41593-019-0520-2>. Bandiera_abtest: a Cg-type: Nature Research Journals Number: 11 Primary_atype: Reviews Publisher: Nature Publishing Group Subject_term: Learning algorithms;Machine learning;Neural circuits Subject_term_id: learning-algorithms;machine-learning;neural-circuit.
- [61] Powers, W. T. Feedback: Beyond Behaviorism Stimulus-response laws are wholly predictable within a control-system model of behavioral organization. *Science* **179**, 351–356 (1973). URL <http://www.sciencemag.org/content/179/4071/351>.
- [62] Powers, W. T. *Behavior: The Control of Perception (2nd ed. rev. & exp.)*, vol. xiv (Benchmark Press, New Canaan, CT, US, 2005).
- [63] Adams, R. A., Shipp, S. & Friston, K. J. Predictions not commands: active inference in the motor system. *Brain Structure and Function* **218**, 611–643 (2013). URL <http://link.springer.com/10.1007/s00429-012-0475-5>.
- [64] Mileusnic, M. P., Brown, I. E., Lan, N. & Loeb, G. E. Mathematical Models of Proprioceptors. I. Control and Transduction in the Muscle Spindle. *Journal of Neurophysiology* **96**, 1772–1788 (2006). URL <https://www.physiology.org/doi/10.1152/jn.00868.2005>.
- [65] Mountcastle, V. B. The columnar organization of the neocortex. *Brain* **120**, 701–722 (1997). URL <https://academic.oup.com/brain/article/120/4/701/372118>.
- [66] Porr, B. & Wörgötter, F. Strongly Improved Stability and Faster Convergence of Temporal Sequence Learning by Using Input Correlations Only. *Neural Computation* **18**, 1380–1412 (2006). URL <https://doi.org/10.1162/neco.2006.18.6.1380>.
- [67] Shafi, M. *et al.* Variability in neuronal activity in primate cortex during working memory tasks. *Neuroscience* **146**, 1082–1108 (2007). URL <http://www.sciencedirect.com/science/article/pii/S0306452206017593>.
- [68] Steinmetz, N. A., Zatka-Haas, P., Carandini, M. & Harris, K. D. Distributed coding of choice, action and engagement

across the mouse brain. *Nature* **576**, 266–273 (2019). URL <https://www.nature.com/articles/s41586-019-1787-x>. Number: 7786 Publisher: Nature Publishing Group.

[69] Najafi, F. *et al.* Excitatory and Inhibitory Subnetworks Are Equally Selective during Decision-Making and Emerge Simultaneously during Learning. *Neuron* **105**, 165–179.e8 (2020). URL <https://www.sciencedirect.com/science/article/pii/S0896627319308487>.

[70] Berg, R. W., Alaburda, A. & Hounsgaard, J. Balanced Inhibition and Excitation Drive Spike Activity in Spinal Half-Centers. *Science* **315**, 390–393 (2007). URL <https://science.sciencemag.org/content/315/5810/390>.

[71] Berg, R. W., Willumsen, A. & Lindn, H. When networks walk a fine line: balance of excitation and inhibition in spinal motor circuits. *Current Opinion in Physiology* **8**, 76–83 (2019). URL <https://www.sciencedirect.com/science/article/pii/S2468867319300069>.

[72] Goulding, M., Bourane, S., Garcia-Campmany, L., Dalet, A. & Koch, S. Inhibition downunder: an update from the spinal cord. *Current Opinion in Neurobiology* **26**, 161–166 (2014). URL <http://www.sciencedirect.com/science/article/pii/S0959438814000567>.

[73] Cowan, J. D., Neuman, J. & van Drongelen, W. WilsonCowan Equations for Neocortical Dynamics. *The Journal of Mathematical Neuroscience* **6**, 1 (2016). URL <https://doi.org/10.1186/s13408-015-0034-5>.

[74] Petersen, P. C., Vestergaard, M., Jensen, K. H. R. & Berg, R. W. Pre-motor spinal network with balanced excitation and inhibition during motor patterns has high resilience to structural division. *The Journal of Neuroscience: The Official Journal of the Society for Neuroscience* **34**, 2774–2784 (2014).

[75] Pierrot-Deseilligny, E. & Burke, D. *The Circuitry of the Human Spinal Cord: Its Role in Motor Control and Movement Disorders* (Cambridge University Press, Cambridge, 2005). URL <https://www.cambridge.org/core/books/circuitry-of-the-human-spinal-cord/BBDFC31B44453B>

[76] Nishimura, Y., Perlmutter, S. I., Eaton, R. W. & Fetz, E. E. Spike-Timing-Dependent Plasticity in Primate Corticospinal Connections Induced during Free Behavior. *Neuron* **80**, 1301–1309 (2013). URL <https://www.sciencedirect.com/science/article/pii/S0896627313007629>.

[77] Bizzi, E. & Ajemian, R. From motor planning to execution: a sensorimotor loop perspective. *Journal of Neurophysiology* **124**, 1815–1823 (2020). URL <https://journals.physiology.org/doi/full/10.1152/jn.00715.2019>. Publisher: American Physiological Society.

[78] Kaufman, M. T., Churchland, M. M., Ryu, S. I. & Shenoy, K. V. Cortical activity in the null space: permitting preparation without movement. *Nature Neuroscience* **17**, 440–448 (2014). URL <https://www.nature.com/articles/nn.3643>. Bandiera_abtest: a Cg-type: Nature Research Journals Number: 3 Primary_atype: Research Publisher: Nature Publishing Group Subject_term: Motor cortex;Premotor cortex Subject_term_id: motor-cortex;premotor-cortex.

[79] Bastian, A. J., Martin, T. A., Keating, J. G. & Thach, W. T. Cerebellar ataxia: abnormal control of interaction torques across multiple joints. *Journal of Neurophysiology* **76**, 492–509 (1996). URL <https://journals.physiology.org/doi/abs/10.1152/jn.1996.76.1.492>. Publisher: American Physiological Society.

[80] Becker, W. J., Morrice, B. L., Clark, A. W. & Lee, R. G. Multi-Joint Reaching Movements and Eye-Hand Tracking in Cerebellar Incoordination: Investigation of a Patient with Complete Loss of Purkinje Cells. *Canadian Journal of Neurological Sciences* **18**, 476–487 (1991). URL <https://www.cambridge.org/core/journals/canadian-journal-of-neurological-sciences/article/multi-joint-reaching-movements-and-eye-hand-tracking-in-cerebellar-incoordination-investigation-of-a-patient-with-complete-loss-of-purkinje-cells/10.1017/S0317167100092000>. Publisher: Cambridge University Press.

[81] Gilman, S., Carr, D. & Hollenberg, J. Kinematic effects of deafferentiation and cerebellar ablation. *Brain* **99**, 311–330 (1976). URL <https://doi.org/10.1093/brain/99.2.311>.

[82] Day, B. L., Thompson, P. D., Harding, A. E. & Marsden, C. D. Influence of vision on upper limb reaching movements in patients with cerebellar ataxia. *Brain* **121**, 357–372 (1998). URL <https://doi.org/10.1093/brain/121.2.357>.

[83] Lillicrap, T. & Scott, S. Preference Distributions of Primary Motor Cortex Neurons Reflect Control Solutions Optimized for Limb Biomechanics. *Neuron* **77**, 168–179 (2013). URL <http://www.sciencedirect.com/science/article/pii/S0896627312009920>.

[84] Kurtzer, I., Pruszynski, J. A., Herter, T. M. & Scott, S. H. Primate Upper Limb Muscles Exhibit Activity Patterns That Differ From Their Anatomical Action During a Postural Task. *Journal of Neurophysiology* **95**, 493–504 (2006). URL <https://journals.physiology.org/doi/full/10.1152/jn.00706.2005>. Publisher: American Physiological Society.

[85] Chambers, A. R. & Rumpel, S. A stable brain from unstable components: Emerging concepts and implications for neural computation. *Neuroscience* **357**, 172–184 (2017). URL <http://www.sciencedirect.com/science/article/pii/S0306452217304013>.

[86] Kalidindi, H. T. *et al.* Rotational dynamics in motor cortex are consistent with a feedback controller. *eLife* **10**, e67256 (2021). URL

<https://doi.org/10.7554/eLife.67256>. Publisher: eLife Sciences Publications, Ltd.

- [87] DeWolf, T., Stewart, T. C., Slotine, J.-J. & Eliasmith, C. A spiking neural model of adaptive arm control. *Proceedings of the Royal Society B: Biological Sciences* (2016). URL <https://royalsocietypublishing.org/doi/abs/10.1098/rspb.2016.2134>. Publisher: The Royal Society.
- [88] Edelman, G. M. & Gally, J. A. Degeneracy and complexity in biological systems. *Proceedings of the National Academy of Sciences* **98**, 13763–13768 (2001). URL <https://www.pnas.org/doi/full/10.1073/pnas.231499798>. Publisher: Proceedings of the National Academy of Sciences.
- [89] Sanguineti, V. *et al.* Cerebellar ataxia: Quantitative assessment and cybernetic interpretation. *Human Movement Science* **22**, 189–205 (2003). URL <https://www.sciencedirect.com/science/article/pii/S0167945702001598>.
- [90] Richter, S. *et al.* Adaptive Motor Behavior of Cerebellar Patients During Exposure to Unfamiliar External Forces. *Journal of Motor Behavior* **36**, 28–38 (2004). URL <https://doi.org/10.3200/JMBR.36.1.28-38>. Publisher: Routledge eprint: <https://doi.org/10.3200/JMBR.36.1.28-38>.
- [91] Verduzco-Flores, S. & De Schutter, E. Draculab: A Python Simulator for Firing Rate Neural Networks With Delayed Adaptive Connections. *Frontiers in Neuroinformatics* **13** (2019). URL <https://www.frontiersin.org/articles/10.3389/fninf.2019.00018/full>.
- [92] Lin, C.-C. K. & Crago, P. E. Neural and Mechanical Contributions to the Stretch Reflex: A Model Synthesis. *Annals of Biomedical Engineering* **30**, 54–67 (2002). URL <https://doi.org/10.1114/1.1432692>.
- [93] Cheah, C. C., Liu, C. & Slotine, J. J. E. Adaptive Tracking Control for Robots with Unknown Kinematic and Dynamic Properties. *The International Journal of Robotics Research* **25**, 283–296 (2006). URL <https://doi.org/10.1177/0278364906063830>. Publisher: SAGE Publications Ltd STM.
- [94] Sanner, R. & Slotine, J.-J. Gaussian networks for direct adaptive control. *IEEE Transactions on Neural Networks* **3**, 837–863 (1992). Conference Name: IEEE Transactions on Neural Networks.
- [95] Bekolay, T. *et al.* Nengo: a Python tool for building large-scale functional brain models. *Frontiers in Neuroinformatics* **7** (2014). URL <https://www.frontiersin.org/articles/10.3389/fninf.2013.00048/full>.

[96] Dura-Bernal, S. *et al.* Cortical Spiking Network Interfaced with Virtual Musculoskeletal Arm and Robotic Arm. *Frontiers in Neurorobotics* **9**, 13 (2015). URL <https://www.frontiersin.org/article/10.3389/fnbot.2015.00013>.

[97] Li, W., Todorov, E. & Pan, X. Hierarchical Feedback and Learning for Multi-joint Arm Movement Control. In *2005 IEEE Engineering in Medicine and Biology 27th Annual Conference*, 4400–4403 (2005). ISSN: 1558-4615.

[98] Martin, V., Scholz, J. P. & Schner, G. Redundancy, Self-Motion, and Motor Control. *Neural Computation* **21**, 1371–1414 (2009). URL <https://doi.org/10.1162/neco.2008.01-08-698>.

[99] Caligiore, D., Parisi, D. & Baldassarre, G. Integrating reinforcement learning, equilibrium points, and minimum variance to understand the development of reaching: A computational model. *Psychological Review* **121**, 389–421 (2014). Place: US Publisher: American Psychological Association.

[100] Sutton, R. S. & Barto, A. G. *Reinforcement Learning: An Introduction* (MIT Press, 2018). Google-Books-ID: sWV0DwAAQBAJ.

[101] Feldman, A. G. Once More on the Equilibrium-Point Hypothesis (Model) for Motor Control. *Journal of Motor Behavior* **18**, 17–54 (1986). URL <https://doi.org/10.1080/00222895.1986.10735369>. Publisher: Routledge _eprint: <https://doi.org/10.1080/00222895.1986.10735369>.

[102] Izawa, J., Kondo, T. & Ito, K. Biological arm motion through reinforcement learning. *Biological Cybernetics* **91**, 10–22 (2004). URL <https://doi.org/10.1007/s00422-004-0485-3>.

[103] Mici, L., Parisi, G. I. & Wermter, S. An Incremental Self-Organizing Architecture for Sensorimotor Learning and Prediction. *IEEE Transactions on Cognitive and Developmental Systems* **10**, 918–928 (2018). Conference Name: IEEE Transactions on Cognitive and Developmental Systems.

[104] Tsianos, G. A., Goodner, J. & Loeb, G. E. Useful properties of spinal circuits for learning and performing planar reaches. *Journal of Neural Engineering* **11**, 056006 (2014). URL <https://doi.org/10.1088%2F1741-2560%2F11%2F5%2F056006>.

[105] Sussillo, D. & Abbott, L. F. Generating Coherent Patterns of Activity from Chaotic Neural Networks. *Neuron* **63**, 544–557 (2009). URL <https://www.sciencedirect.com/science/article/pii/S0896627309005479>.

[106] Bashor, D. P. A large-scale model of some spinal reflex circuits. *Biological Cybernetics* **78**, 147–157 (1998). URL <https://doi.org/10.1007/s004220050421>.

[107] Stienen, A. H. A., Schouten, A. C., Schuurmans, J. & van der Helm, F. C. T. Analysis of reflex modulation with a biologically realistic neural network. *Journal of Computational Neuroscience* **23**, 333 (2007). URL <https://doi.org/10.1007/s10827-007-0037-7>.

[108] Cutsuridis, V. Does abnormal spinal reciprocal inhibition lead to co-contraction of antagonist motor units? a modeling study. *International Journal of Neural Systems* **17**, 319–327 (2007). URL <https://www.worldscientific.com/doi/abs/10.1142/S0129065707001160>. Publisher: World Scientific Publishing Co.

[109] Cisi, R. R. L. & Kohn, A. F. Simulation system of spinal cord motor nuclei and associated nerves and muscles, in a Web-based architecture. *Journal of Computational Neuroscience* **25**, 520–542 (2008). URL <https://doi.org/10.1007/s10827-008-0092-8>.

[110] Farina, D., Negro, F. & Dideriksen, J. L. The effective neural drive to muscles is the common synaptic input to motor neurons. *The Journal of Physiology* **592**, 3427–3441 (2014). URL <https://physoc.onlinelibrary.wiley.com/doi/abs/10.1113/jphysiol.2014.273581>. eprint: <https://physoc.onlinelibrary.wiley.com/doi/pdf/10.1113/jphysiol.2014.273581>.

[111] Shevtsova, N. A. *et al.* Organization of left/right coordination of neuronal activity in the mammalian spinal cord: Insights from computational modelling. *The Journal of Physiology* **593**, 2403–2426 (2015). URL <https://physoc.onlinelibrary.wiley.com/doi/abs/10.1113/JP270121>. eprint: <https://physoc.onlinelibrary.wiley.com/doi/pdf/10.1113/JP270121>.

[112] Shevtsova, N. A. & Rybak, I. A. Organization of flexorextensor interactions in the mammalian spinal cord: insights from computational modelling. *The Journal of Physiology* **594**, 6117–6131 (2016). URL <https://www.ncbi.nlm.nih.gov/pmc/articles/PMC5088238/>.

[113] Danner, S. M., Shevtsova, N. A., Frigon, A. & Rybak, I. A. Computational modeling of spinal circuits controlling limb coordination and gaits in quadrupeds. *eLife* **6**, e31050 (2017). URL <https://doi.org/10.7554/eLife.31050>. Publisher: eLife Sciences Publications, Ltd.

[114] Zelenin, P. V. *et al.* Differential Contribution of V0 Interneurons to Execution of Rhythmic and Nonrhythmic Motor Behaviors. *The Journal of Neuroscience: The Official Journal of the Society for Neuroscience* **41**, 3432–3445 (2021).

[115] Stachowski, N. J. & Dougherty, K. J. Spinal Inhibitory Interneurons: Gatekeepers of Sensorimotor Pathways. *International Journal of Molecular Sciences* **22**, 2667 (2021). URL <https://www.ncbi.nlm.nih.gov/pmc/articles/PMC7961554/>.

[116] Borisyuk, R., Azad, A., Conte, D., Roberts, A. & Sofie, S. Modeling the Connectome of a Simple Spinal Cord. *Frontiers in Neuroinformatics* **5**, 20 (2011). URL <https://www.frontiersin.org/article/10.3389/fninf.2011.00020>.

[117] Cangiano, L. & Grillner, S. Mechanisms of Rhythm Generation in a Spinal Locomotor Network Deprived of Crossed Connections: The Lamprey Hemicord. *Journal of Neuroscience* **25**, 923–935 (2005). URL <https://www.jneurosci.org/content/25/4/923>. Publisher: Society for Neuroscience Section: Behavioral/Systems/Cognitive.

[118] Zappacosta, S., Mannella, F., Mirolli, M. & Baldassarre, G. General differential Hebbian learning: Capturing temporal relations between events in neural networks and the brain. *PLOS Computational Biology* **14**, e1006227 (2018). URL <https://journals.plos.org/ploscompbiol/article?id=10.1371/journal.pcbi.1006227>. Publisher: Public Library of Science.

[119] Fiete, I. R., Senn, W., Wang, C. Z. H. & Hahnloser, R. H. R. Spike-Time-Dependent Plasticity and Heterosynaptic Competition Organize Networks to Produce Long Scale-Free Sequences of Neural Activity. *Neuron* **65**, 563–576 (2010). URL <https://www.sciencedirect.com/science/article/pii/S0896627310000917>.

[120] Kaleb, K., Pedrosa, V. & Clopath, C. Network-centered homeostasis through inhibition maintains hippocampal spatial map and cortical circuit function. *Cell Reports* **36**, 109577 (2021). URL <https://www.sciencedirect.com/science/article/pii/S2211124721010111>.

[121] Lim, S. & Goldman, M. S. Balanced cortical microcircuitry for maintaining information in working memory. *Nature Neuroscience* **16**, 1306–1314 (2013). URL <https://www.nature.com/articles/nn.3492>. Bandiera_abtest: a Cg_type: Nature Research Journals Number: 9 Primary_atype: Research Publisher: Nature Publishing Group Subject_term: Network models Subject_term_id: network-models.

[122] Helmchen, F. Dendrites as biochemical compartments. In *Dendrites*, 376 (Oxford University Press, Oxford, England, 1999). URL https://pure.mpg.de/pubman/faces/ViewItemOverviewPage.jsp?itemId=item_2537436.

[123] Kawato, M., Ohmae, S., Hoang, H. & Sanger, T. 50 years since the Marr, Ito, and Albus models of the cerebellum. *arXiv:2003.05647 [q-bio]* (2020). URL <http://arxiv.org/abs/2003.05647>. ArXiv: 2003.05647.

SUPPLEMENTARY INFORMATION

6 Supplementary Discussion

6.1 Comparison with previous models

There are many other models of reaching and motor control. Most of them have one or more of the following limitations:

1. They use non-neural systems to produce motor commands.
2. They control a single degree of freedom, sidestepping the problem of controller configuration, since the error is one-dimensional.
3. They do not model a biologically plausible form of synaptic learning.

We will contrast our model with some of the work that does not strongly present these limitations, and with a few others. Due to space limitations, the contributions of many models will not be addressed, and, for those mentioned, we will limit ourselves to explain some of their limitations.

The model in [87] is similar has similar goals to our model, but with very different assumptions. In their model, motor cortex receives a location error vector x , and transforms it into a vector of joint torques. So that this transformation implements adaptive kinematics, it must approximate a Jacobian matrix that includes the effects of the arm's inertia matrix, using location errors and joint velocities as training signals. This is accomplished by adapting an algorithm taken from the robotics literature [93], implementing it in a spiking neural network. Additionally a second algorithm from robotics [94] is used to provide an adaptive dynamics component, which is interpreted as the cerebellar contributions.

In order to implement vector functions in spiking neural networks [87] uses the Neural Engineering Framework [95]. The essence of this approach is to represent values in populations of neurons with cosine-like tuning functions. These populations implement expansive recoding, becoming a massively overcomplete basis of the input space. Implementing a function using this population as the input is akin to using a linear decoder to extract the desired function values from the population activity. This can be done through standard methods, such as least-squares minimization, or random gradient descent. The parameters of the linear decoder then become weights of a feedforward neural layer implementing the function.

The model in [87] has therefore a rather different approach. They use engineering techniques to create a powerful motor control system, using algorithms from robotics, and 30,000 neurons to approximate their computations, which are then ascribed to sensory, motor, and premotor cortices, as well as the cerebellum. In contrast, we use 74 firing rate units, and unlike [87] we include muscles, muscle afferents, transmission delays, and a spinal cord.

There is nothing intrinsically wrong with using an engineering approach to try to understand a biological function. The crucial part is which model will

be experimentally validated. Some differences between the models that may be able to separate them experimentally are: 1) In [87] premotor cortex is required to produce the error signal, whereas we ascribed this to sensory cortex. 2) In [87] direct afferent connections to motor cortex are not considered, whereas in our model they are necessary to maintain stability during learning (in the absence of a cerebellum). 3) In [87] spinal cord adaptation is not necessary to implement adaptive kinematics. In contrast, spinal cord adaptation is the basis of our model.

The model in [96] uses spiking neurons, and a realistic neuromechanical model in order to perform 2D reaching. The feedback is in term of muscle lengths, rather than muscle afferent signals. There is no mechanism to stop the arm, or hold it on target. Most importantly, learning relies on a critic, sending rewarding or punishing signals depending on whether the hand was approaching or getting away from the target. This is implicitly reducing the error dimension using a hidden mechanism. Furthermore, each single target must be trained individually, and it is not discussed how this can lead to a flexible reaching mechanism without suffering from catastrophic interference.

The model in [35] is used to obtain characteristics of M1 activity given the required muscle forces to produce a movement. It is an open-loop, locally-linear model, where all connections from M1 directly stimulate a linear motoneuron. Among other things, it showed that representations of kinematic parameters can appear when the viscoelastic properties of the muscles are taken into account, giving credence to the hypothesis that M1 directly activates muscle groups. Outside of its scope are neural implementation, learning, or the role of spinal cord.

[97] proposes a 2-level hierarchical controller for a 2-DOF arm. Since this model is based on optimal control theory, it is given a cost function, and proceeds by iteratively approaching a solution of the associated Jacobi-Bellman equation. There is no neural implementation of these computations, nor a description of learning.

[98] is not properly a neural model, but it is rooted in Dynamic Field Theory, which assumes that the population of neuronal activities encodes "activation variables". For this model activation variables represent kinematic parameters as a virtual joint location vector $\lambda(t)$, which is an internal representation of the arm's configuration.

The innovative part of [98] is in describing how $\lambda(t)$ is updated and used to control a redundant manipulator. In particular, the kinematic Jacobian, its null-space matrix, their derivatives, and the Moore-Penrose pseudoinverse are all computed analytically in order to obtain differential equations where the joint motions that move the end effector decouple from those which don't.

Encapsulating the muscle commands into a virtual joint location whose dynamics are decoupled for motions that don't affect the end-effector location is a very interesting concept. Still, this is far from a neural implementation, and learning is not considered.

The model in [99] studies the long-term development of infant reaching using a PD controller, and an actor critic mechanism implementing a neural version of

TD-learning [100]. The 2-dimensional PD controller receives two desired joint angles (interpreted as an equilibrium position), producing appropriate torques. Since it uses the Equilibrium Point (EP) Hypothesis [101], the reaching portion of this model is tantamount to associating states with equilibrium positions. This model thus performs at a higher level of analysis. Our model could operate at the same level if we added a reinforcement learning component to learn S_P values allowing the hand to *touch* a target whose distance is known. [99] does not consider separate neuronal populations (e.g. spinal cord, sensory cortex), propagation delays, or low-level learning.

The model in [102] shows how reinforcement learning can be applied to redundant actuators, such as biological arms. It is, however, not a neural model.

In [103], a neural network produces predictions of visual input in order to deal with temporal delays in a sensorimotor system. The network used for this study uses non-local learning, and adds or destroys nodes as required during its operation. It is thus not biologically-plausible.

[104] is a reaching model that also considers the spinal cord as a highly-configurable controller. Corticospinal inputs are assumed to be step commands, which means that motor cortex operates in an open-loop configuration. In order to produce reaching based on these constant commands, a biologically-implausible gradient descent mechanism is required, where the same reach is performed for various values of a synaptic weight, keeping the value that led to the best performance. Furthermore, the model learns to reach one target at a time, which would require learning anew when the new target is more than 45 degrees apart.

As mentioned in the main text, in the context of rotational dynamics, the model in [40] was used to produce desired muscle forces using a recurrent neural network. This model uses the FORCE algorithm [105] to adjust the weights of a neural network with activity vector $\mathbf{r}(t)$ so it can produce experimentally observed muscle activity $\mathbf{m}(t)$. Oscillatory dynamics arise when the model is constrained to be simple.

Although very insightful, this model is limited by the fact that equations 2 and 3 represent an open-loop configuration, where only the M1 dynamics are considered. In essence, the model is doing a function approximation with the FORCE algorithm. The question of how the training data $\mathbf{m}(t)$ is produced is not addressed, nor is the role of spinal cord or sensory cortex (but see their Supplementary Figure 1).

Other than the aforementioned model in [104], we are unaware of spinal cord models addressing arm reaching. When these models are coupled with a musculoskeletal system, it is usually for the control of one degree of freedom using antagonistic neural populations. We mention some examples next.

The spinal cord model in [106] inspired much of the subsequent work, organizing the spinal circuit into six pairs of populations controlling two antagonistic muscle groups at one joint. With this model, the effect of Ia and Ib afferent input was studied in various neuronal populations.

[107] used a model similar to that in [106] in conjunction with a one DOF musculoskeletal model to study the effect of Ia afferents in the modulation of

reflexes. [108] also adapted a similar model, and used it to inquire whether Parkinsonian rigidity arose from alterations in reciprocal inhibition mediated by reduced dopamine.

The model in [109] has several features not found in [106], including a heterogeneous motoneuron population, and a mechanism to generate electromyograms. This was used to study the generation of the H-reflex, and response properties of the motor neuron pool [110].

The model in [111] goes beyond models such as [106] by using populations of genetically-identified interneurons. This model is used to study rhythm generating abilities of the spinal circuit, as well as coordination between flexors and extensors [112, 113]. Knowledge regarding the role of genetically identified spinal interneurons in movement generation is still evolving [114, 115, e.g.].

This paper focuses on mammals, but the spinal cord of simpler organisms is better characterized [116, 117, e.g.], and may lead to the first realistic models producing ethological behavior.

6.2 Possible implementations of the learning rule

The learning rule in equation 9 is a Hebbian rule that also presents derivatives, heterosynaptic competition, and normalization (e.g. removing the mean) of its terms. None of these is new in a model claiming biological plausibility (e.g. [66, 118, 119, 120]). We nevertheless mention possible ways for derivatives and normalized terms to appear.

Formally, the time derivative of a function $f : \mathbb{R} \rightarrow \mathbb{R}$ evaluated at time t is the limit $\frac{f(t+\Delta t) - f(t)}{\Delta t}$ as $\Delta t \rightarrow 0$. If f represents the firing rate of a cell, a measure of change roughly proportional to the derivative can come from $f(t) - f(t - \Delta t)$ for some small value Δt . The most obvious way that such a difference may arise is through feedforward inhibition (for the e_j signal), and feedback inhibition (for the c_i signal). Feedforward and feedback inhibition are common motifs in spinal circuits [75].

A somewhat different way to approach a time derivative is by using two low-pass filters with different time constants:

$$\frac{df}{dt} \approx f_{fast}(t) - f_{slow}(t),$$

where

$$\begin{aligned} \tau_1 \dot{f}_{fast}(t) &= f(t) - f_{fast}(t), \\ \tau_2 \dot{f}_{slow}(t) &= f(t) - f_{slow}(t), \\ \tau_2 &\gg \tau_1. \end{aligned}$$

These principles are illustrated in [121] , where they are used to explain negative-derivative feedback.

Low-pass filtering can also arise in the biochemical cascades following synaptic depolarization. The most salient case is intracellular calcium concentration,

which has been described as an indicator of firing rate with leaky integrator dynamics [122]. Although the physiology of spinal interneurons has not been characterized with sufficient detail to make specific hypotheses, it is clearly possible that feedback inhibition and low-pass filtering are enough to approximate a second-order derivative.

The e_j, c_i terms in our learning rule are mean-centered. The most straightforward way to subtract a mean is to have inhibitory units with converging inputs (e.g. receiving all the e_j signals) providing input to the c_i units. The Ib interneurons [75] are one possibility for mediating this. Another possibility is that the mean-subtraction happens at the single unit level when the input (e_j) and lateral (c_i) connections are located at different parts of the dendritic tree. In particular, a larger level of overall input activation $\langle \bar{e} \rangle$ could produce a scarcity of postsynaptic resources flowing from the main branches of the dendritic tree into the individual dendritic spines, resulting in reduced plasticity.

6.3 Limitations of the model

A model as simple as ours will undoubtedly be wrong in many details. The main simplifying assumptions of our model are:

- **Firing rate encoding.** Each unit in this model captures the mean-field activity of a neuronal population. This may occlude computations depending on spike timing, as well as fine-grained computations at the neuronal and dendritic level.
- **Trivial sensory cortex.** We assumed that sensory cortex conveyed errors directly based on static gamma afferent activity. Sensory cortex may instead build complex representations of afferent activity. It would be interesting to test how the requirement of controllability could guide learning of these representations.
- **No visual information.** Should a visual error be available, it could be treated by M in a similar way to somatosensory errors. If the visual error holds a monotonic relation with the afferent signals, then it should be possible to adjust the long-loop reflex in order to reduce it. When the relation between the visual error and the afferent signals is not monotonic (e.g. in some context the afferent signals correlate positively, and in other negatively), an alternative approach involving reinforcement learning can be pursued [11].
- **Very gross anatomical detail.** The detailed anatomical organization of cortex and spinal cord is not considered. Moreover, the proportions for different types of cells are not considered.
- **Errors must be monotonic.** Muscle activation may not monotonically reduce visual errors. Moreover, the haptic perception of contact is dependent on the environment, so it would not make an appropriate error signal.

- **No cerebellum, basal ganglia, or premotor cortex.**

Each of these omissions is also a possible route for improving the model. We aim to grow a more sophisticated model, but each new component must integrate with the rest, improve functionality and agree with biological literature.

A final limitation concerns proofs of convergence. Many factors complicate them for this model: transmission delays, noise, synaptic learning, fully neural implementation, as well as complex muscle and afferent models. We tested our results for many initial conditions, but this of course is no guarantee.

50 years ago Marr’s model of the cerebellum became a stepping stone to further theoretical and experimental progress, despite all its shortcomings [123]. We aspire our model to be the next step towards a complete model of motor control.

7 The model fails when elements are removed

Due to the larger number of tests, we only used 5 trials for each configuration in this section. The p values reported in this section come from the one-sided t-test.

A model with fully random connectivity and no plasticity has an exceedingly low probability of having an input-output structure leading it to reduce errors. The configurations of the model with plasticity (configurations 1,2,4,5), however, only have random connections at one of the projections in the sensorimotor loop (either from M to C , or from S_{PA} to M). This may increase the chance of randomly obtaining a good input-output structure, which could throw the usefulness of the learning rules into question.

Removing both types of plasticity in configurations 1,2,4,5 impaired reaching in all 5 tests for each configuration, as reflected by the inability to reduce the average error below 10 centimeters in any of the last 4 reaches of the learning phase. This was also true when removing only the plasticity in the connections from M to C (configurations 1, 4, 5) or from S_{PA} to M (configuration 2). In each one of the plastic configurations (1,2,4,5) the average error for the last 4 training targets was $(22 \pm 10, 22 \pm 4, 24 \pm 9, 22 \pm 5)$ centimeters, which was significantly higher than the case with normal plasticity ($p < 0.001$ for configurations 2,4,5, $p = 0.028$ for configuration 1, where the failed trials were not discarded).

Removing plasticity in the connections from A to C or from A to M individually had for the most part no statistically significant effects. Removing plasticity in both connections simultaneously, however, roughly duplicated the error in configurations 2 and 4 during center-out reaching (one-sided t-test, $p < 0.001$). Error may be slightly increased for configuration 1 (the small sample size allowed no strong conclusions), whereas configuration 5 was seemingly unaffected.

Configurations (1,2,4,5) could still learn to reach after removing the ACT unit. Configuration 4 roughly duplicated its center-out reaching error ($p < 0.001$) and its time to initially reach ($p = .016$). Configuration 1 increased its

time to initially reach about 3 times ($p < 0.001$), and the other two configurations were seemingly unaffected. The *ACT* unit was essential for previous, less robust versions of the model.

Removing noise made learning too slow, to the point where mean error in the last 4 training reaches could not be reduced below 10 cm in any trial for configurations 4, and 5. It was reduced below 10 cm in a single trial for configuration 2. Configuration 1 managed to learn normally. Center-out reaches were not possible in configurations 2, 4, and 5 with mean errors of $(15 \pm 8, 17 \pm 11, 9 \pm 3)$ centimeters respectively, at least 3 times larger than the models with noise ($p < 0.001$). Center-out reaches were normal in configuration 1, but the first reach with mean error below 10 centimeters took significantly longer to happen (from 2.5 to 6.4 attempts in average, $p = 0.001$).

Removing Ia and Ib afferents, and instead sending the output of II afferents to C , M , and S_A prevented reaching in configurations 1, 2, 3, and 4 (except for a single trial in configuration 1). Configuration 5 could still learn to reach, but the mean error in the last 4 training reaches and during the center-out reaching was significantly higher ($p < 0.001$).

Removing the agonist-antagonist connections in C prevented reaching in (5, 0, 0, 3, 2) trials for configurations (1,2,3,4,5) respectively. Error in center-out reaching was significantly increased for configurations 4 and 5, and it did not increase significantly for configurations 2 and 3.

Figure S6 is the same as figure 2, but in this case the noise and the ACT units were both removed. The average distance from the hand to the target was roughly 18 cm. A video illustrating this failure to learn is included in the supplementary materials (section 10).

Configuration 1 was resilient to removal of noise and the ACT unit individually. The simulation of figure S6 suggests that removing more than one element will have larger consequences on the performance of the model.

8 Comparison of the 5 configurations

The 5 configurations (or models) in this paper are represented by a number. The following table shows the connectivity in each one. Abbreviations: A2A: all-to-all, O2O: one-to-one, DH: the differential Hebbian learning rule from [11], IC: the Input Correlation learning rule, S: static connections (see section 4.5 for details on the weights of static connections).

Configuration	S_{PA} to M	M to C	A to C, M
1	O2O, S	A2A, DH	A2A, IC
2	A2A, DH	S	A2A, IC
3	O2O, S	S	S
4	O2O, S	A2A, DH	A2A, IC
5	S	A2A, DH	A2A, IC

- Configuration 1 is a “basic” network where the input-output structure of the control loop happens in the spinal cord, in the connections from M to

C .

- Configuration 2 is also a “basic” network, but the input-output structure is resolved in the intracortical connections from S_{PA} to M .
- Configuration 3 uses only static connections, and is meant to show that the results in the paper appear in a close to optimal configuration of feedback control, rather than being some sophisticated product of the plasticity rules.
- Configuration 4 is an extension of configuration 1, where the spinal cord has 12 CE, CI pairs rather than 6, and each pair stimulates 2 α motoneurons.
- Configuration 5 is a different variation of configuration 1, where the connections from S_{PA} to M are not one-to-one, but instead come from an orthogonal matrix.

The following table summarizes the numerical results for the 5 configurations.

Measurement	1	2	3	4	5
Failed reaches ¹	1.8 ± 2	$1.2 \pm .9$	0 ± 0	1.6 ± 1.3	4 ± 2.5
Center-out error ²	$3.3 \pm .01$	$2.9 \pm .001$	$2.9 \pm .0003$	$3 \pm .008$	$2.8 \pm .0007$
M units tuned to direction	$11.8 \pm .4$	12 ± 0	12 ± 0	12 ± 0	12 ± 0
R^2 for predicted PD	$.74 \pm .18$	$.88 \pm .14$	$.86 \pm .01$	$.89 \pm .06$	$.82 \pm .03$
PD distribution main axis (deg)	59 ± 7	52 ± 2	$54 \pm .5$	60 ± 3	58 ± 1
PD drift angle (deg)	3.3 ± 2.4	4.9 ± 2.1	$.3 \pm .2$	1.8 ± 1.3	7 ± 6
Muscle PD drift angle (deg)	3.8 ± 2.1	6.4 ± 2.9	$.2 \pm .2$	11.4 ± 15.2	27.7 ± 34.5
Center-out error (10 targets)	3	3.6	2.9	2.6	4.5
Variance in first jPCA	$.42 \pm .04$	$.42 \pm .04$	$.46 \pm .03$	$.45 \pm .04$	$.47 \pm .07$
Center-out error (light arm)	2.5	3.2	3	6.1	2.9
Center-out error (heavy arm)	2.4	3.3	2.9	5.6	3.2

¹ Average number of reaches before the first reach when the mean error was below 10 cm.

² Average distance (in centimeters) between the hand and the target during center-out reaching.

9 Gain and oscillations

The gain of a feedback loop describes how the amplitude of the error signal increases as it gets transformed into a control signal sent to the plant. As described in the Methods (section 4.7), we used a relatively low number of iterations of an optimization algorithm to find suitable parameters for each configuration of the model. This led to configurations with gains that were coarsely tuned. Supplementary figure S7 is analogous to figure 3, and shows the hand trajectories right after the optimization algorithm was finished. It can be observed that configurations 2 and 3 were particularly prone to oscillations, and configuration 1 would undershoot many targets.

To improve performance, as well as to facilitate comparison of the 5 configurations, we adjusted their gains. This involved manually adjusting the slope of the sigmoidal units in populations M and S_A , until they appeared stable, but on the verge of oscillating (so reaching would be faster). This required from 1 to 3 attempts. The gain of configuration 1 was slightly increased, whereas the gain of configurations 2,3,4 was reduced. Configuration 5 was left with the same parameters.

The trajectories in panels C and D of figure S7 are reminiscent of terminal tremors in cerebellar ataxia. An animation showing the movement of the arm for the 5 configurations before gain adjustment is included among the Supplementary Videos. In addition, supplementary figures S8 and S9 show the error and activity of several units during the training reaches for configurations 3 and 4, analogous to figure 2. It can be observed that the oscillations are present in the whole network, suggesting that the control signals are trying to catch up with an error that keeps reversing direction.

10 Supplementary videos

To help visualization of the arm’s learning and performance under different conditions, 4 videos were produced. To download these videos, please visit https://gitlab.com/sergio.verduzco/public_materials/, and navigate to the `adaptive_plasticity` folder.

The videos’ content is as follows:

- `learning_config1.mp4`: Visualization of the arm and the muscles during the learning phase for configuration 1. Data comes from the simulation shown in figure 2. Speed is roughly 4X.
- `center_out.mp4`: Arm animation of the first 180 seconds of center-out reaching for the 5 configurations. Speed is roughly 4X.
- `learning_fail.mp4`: The learning phase for a simulation with configuration 1. Both noise and the *ACT* unit were removed, reducing exploration and disrupting learning. Data comes from the same simulation in figure S6. Speed is 4X.

- `center_out_raw_gains.mp4`: The first 180 seconds of center-out reaching for the 5 configurations before the gains were adjusted. Speed is roughly 4X. Configuration 2 shows target-dependent oscillations after 70 seconds.

11 Parameter values

Values appear in order for configurations 1-5. A single number means that all configurations use that same value.

11.1 Unit parameters

The superscript x on a population name indicates that a parameter has heterogeneous values. This means that a random value was added to the parameter for each individual unit. This random value comes from a uniform distribution centered at zero, with a width equal to 1% of the reported parameter value.

Parameter	Equation	Population	Value
τ_u	5	CHG, A, ACT	10 [ms]
		$\alpha, S_A, S_{PA}^x, CI$	20 [ms]
		CE	140, 70, 150, 180, 110 [ms]
		M^x	50 [ms]
β	6	α^x, ACT	2
		CE	1.63, 1.72, 1.70, 3.38, 1.44
		CI	4.0, 3.38, 3.44, 2.46, 3.63
		M^x	1.5, 1.5, 2.0, 2.0, 1.17
		S_A	3.0, 2.2, 2.0, 2.3, 3.0
		CHG, S_{PA}^x	9
η	6	α^x	1.1
		CE	2.0, 1.93, 2.13, 2.31, 1.67
		CI	1.5, 1.41, 1.63, 1.72, 1.7
		M_x	1.3, 1.96, 0.68, 1.19, 1.38
		ACT	1
		S_A	0.75
		units 0,3	
		S_A	.4
		units 1,2,5	
		S_A	.3
		unit 4	
		CHG	.25
		S_{PA}^x	.1
ς	7	CE, CI	0.63, 0, 0, 0.69, 0.72
		M	0, 0.62, 0, 0, 0
τ_a	8	A	10 [ms]
T	8	A	.2
		I_b, II afferents	
		A	0
		I_a afferents	
τ_{slow}	12, 13	CE, CI	11 [s]
θ_{ACT}	15, 16	ACT	.31
τ_{ACT}	16	ACT	10 [ms]
γ	16	ACT	8
α	17	CHG (synapse)	20

11.2 Learning rules

Parameter	Equation	Value
Δt	9	0.33, 0.37, 0.15, 0.36, 0.32 [s]
$\alpha(M \text{ to } C)$	10	500, 0, 0, 500, 500
$\alpha(S_{PA} \text{ to } M)$	10	0, 527, 0, 0, 0
$\alpha(M \text{ to } \alpha)$	10	300, 0, 0, 300, 300
λ	10	.03
$\omega_{sa}(M \text{ to } C, \alpha)$ ¹	10	2.52
$\omega_{sa}(S_{PA} \text{ to } M)$	10	3.23, 3.19, 2.98, 3.23, 3.23
$\omega_{sb}(M \text{ to } C)$	10	3.29, 2.14, 1.50, 3.69, 0.57
$\omega_{sb}(M \text{ to } \alpha)$	10	2.86, 2.86, 1.50, 2.86, 2.86
$\alpha_{IC}(A \text{ to } M)$	11	26.17
$\alpha_{IC}(A \text{ to } C)$	11	22.5
$\omega_s(A \text{ to } M)$	11	0.85, 1.14, 1, 0.53, 0.53
$\omega_s(A \text{ to } C)$	11	1.68, 2, 2, 1.55, 2.88
$\omega_{max}(A \text{ to } M)$	11	.48, .22, .2, .25, .33
$\omega_{max}(A \text{ to } C)$	11	.3, .64, .64, .28, .59

¹ Constraints in the sum of weights are also used with static connections.

11.3 Muscles and afferents

Parameter	Equation	Value
K_{SE}	18	20 [N/m]
K_{PE}	18	20 [N/m]
b	18	1 [N · s / m]
g	18 muscles 0,3	67.11 [N]
g	18 muscles 1,2,4,5	.75 [N]
K_{SE}^s	19,20,21	2 [N/m]
K_{PE}^s	19,20,21	2 [N/m]
b^s	19, 21	.5 [N · s / m]
K_{SE}^d	19,20,21	1 [N/m]
K_{PE}^d	19	.2 [N/m]
b^d	19	2 [N · s / m]
l_0^s	19	.7
l_0^d	19	.8
g_{I_a}	20 muscles 0-5	[7.5, 25, 25, 7.5, 25, 25] [m ⁻¹]
$f_s^{I_a}$	20	0.1
g_{II}	21 muscles 0-5	[5.46, 8, 8, 5.46, 8, 8]*, [5.8, 8, 8, 5.8, 8, 8]** [m ⁻¹]
f_s^{II}	21	0.5
g_{I_b}	22	1
T_0	22	10 [N]
τ_g	23	50 [ms]

11.4 Connection delays and weights

Connections considered "local" used a delay of 10 [ms], unless those connections implied a not-modeled disynaptic inhibition. All other connections had a delay of 20 [ms].

Source	Target	Delay
A	M, S_A	20 [ms]
ACT	CE, CI	
α	muscle	
M	CE, CI, α	
M	M	
afferents	A	
CHG, S_{PA}	ACT	
S_{PA}	M, S_{PA}	
A	M	10 [ms]
CE, CI	α	
CE, CI	CE, CI	
CI	CE	
S_A, S_P	S_{PA}	
S_P	CHG	

The next table shows the value of fixed synaptic weights not specified in section 4.5. Columns indicate the source of the connection, rows indicate the target. "Aff" stands for the muscle afferents. Potentially plastic connections are marked as "+". If a connection marked "+" is static in one of the configurations, its weight is determined by the $\omega_{sa}, \omega_{sb}, \omega_s$ parameters of equations 10, 11.

	α	A	CE	CI	M	Aff.	S_A	S_P	S_{PA}
α			1	-1	+				
A						2 (I_a, I_b), 4 (II)			
ACT									1
CE	+		.5 ^a , .18 ^b	-1.8 ^c	+				
CHG									+
CI	+		.5 ^c 1.83 ^d , .16 ^e		+				
M	+				*				+
muscles	1								
S_A		1					1 or -1	1 or -1	-1.77
S_{PA}									

^a Agonist connections. ^b Partial agonist connections. ^c With the same (CE, CI, α) triplet. ^d Antagonist connections. ^e Partial antagonist connections.

* M units inhibited their duals with weights that depended on the configuration: -0.93, -0.74, -1.00, -1.14, 0.0.

All connections whose source is CHG or ACT have a weight of 1.

12 Supplementary figures

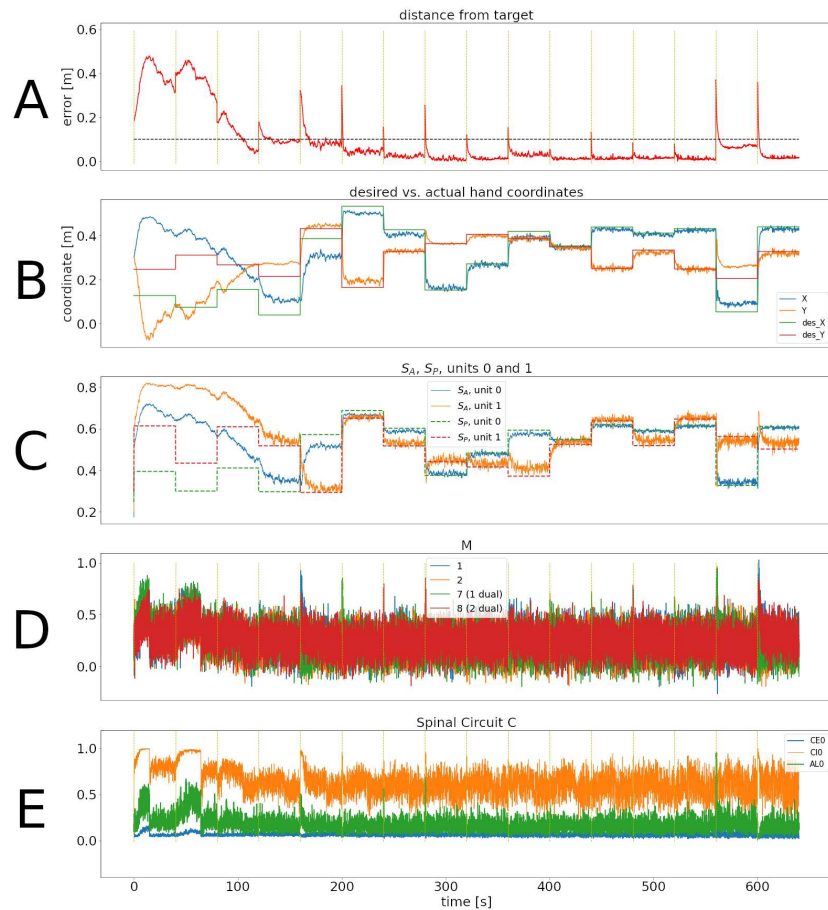


Figure S1: Representative training phase of the simulation for configuration 2. Panels are as in figure 2.

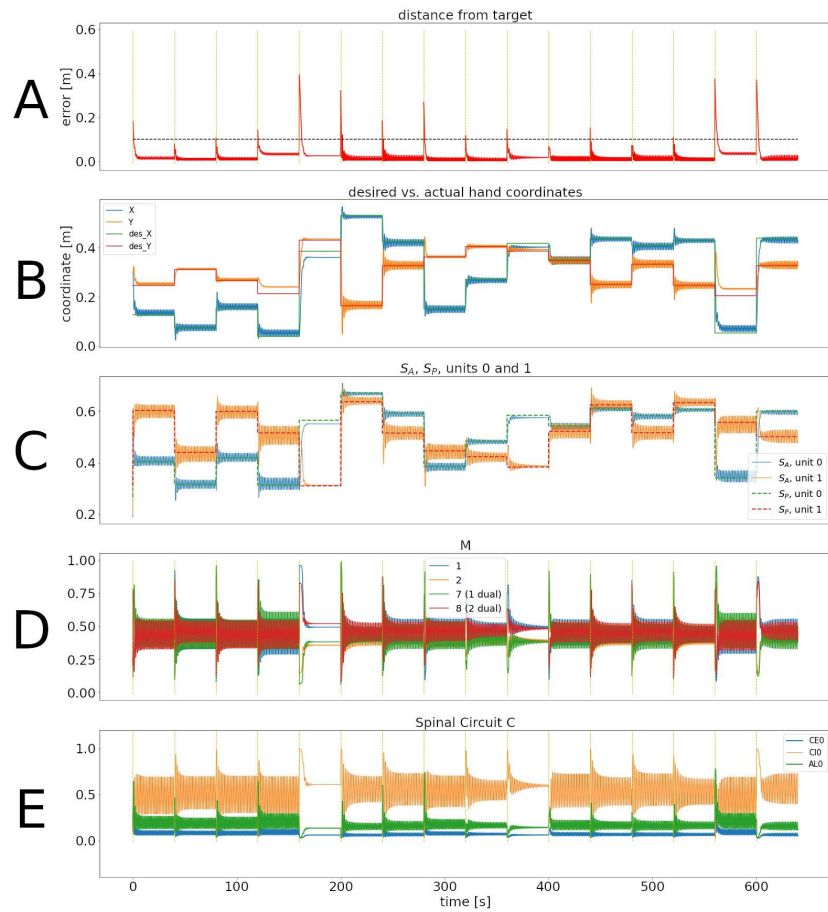


Figure S2: Representative training phase of the simulation for configuration 3. Panels are as in figure 2.

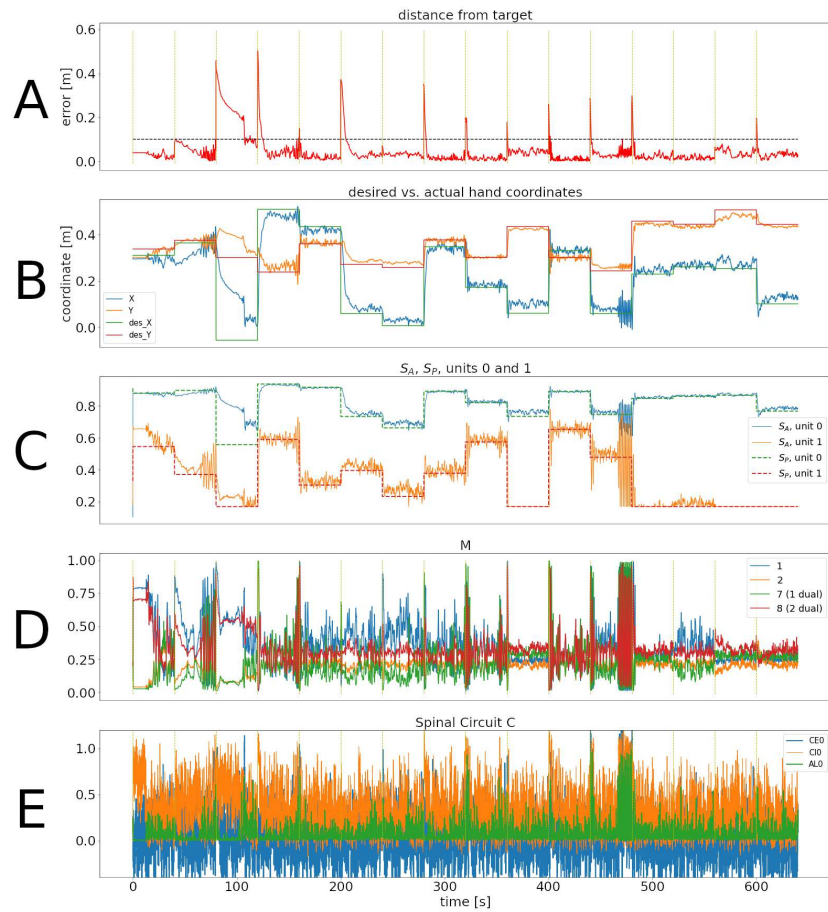


Figure S3: Representative training phase of the simulation for configuration 4. Panels are as in figure 2.

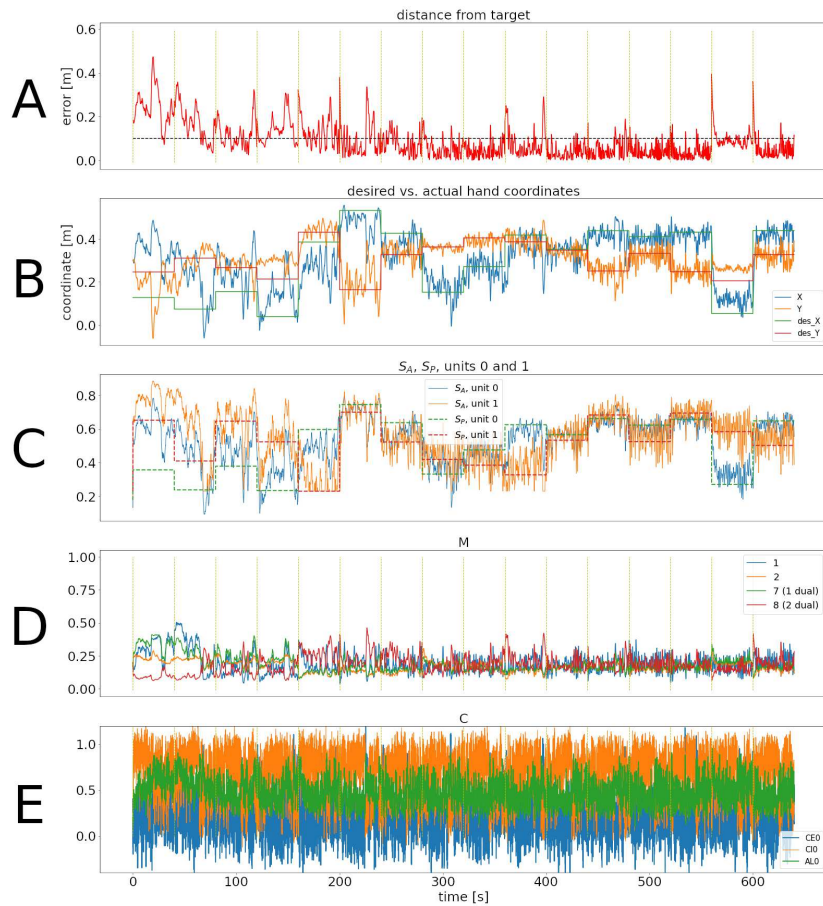


Figure S4: Representative training phase of the simulation for configuration 5. Panels are as in figure 2.

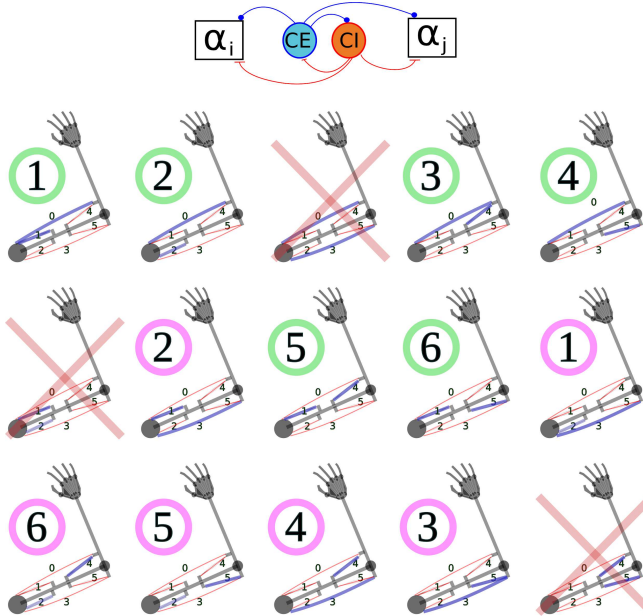


Figure S5: Modified architecture of the C population. Each pair of CE, CI units projects to two α motoneurons (top). There are 15 possible pairs of muscles, corresponding to the blue lines for each arm in the figure. Three of the pairs (marked with red crosses) contain antagonist muscles, and are not included. The remaining 12 pairs can be arranged into 2 groups of 6 units each. The units in the group marked with green circles are the antagonists of the units with the same number, marked with pink circles.

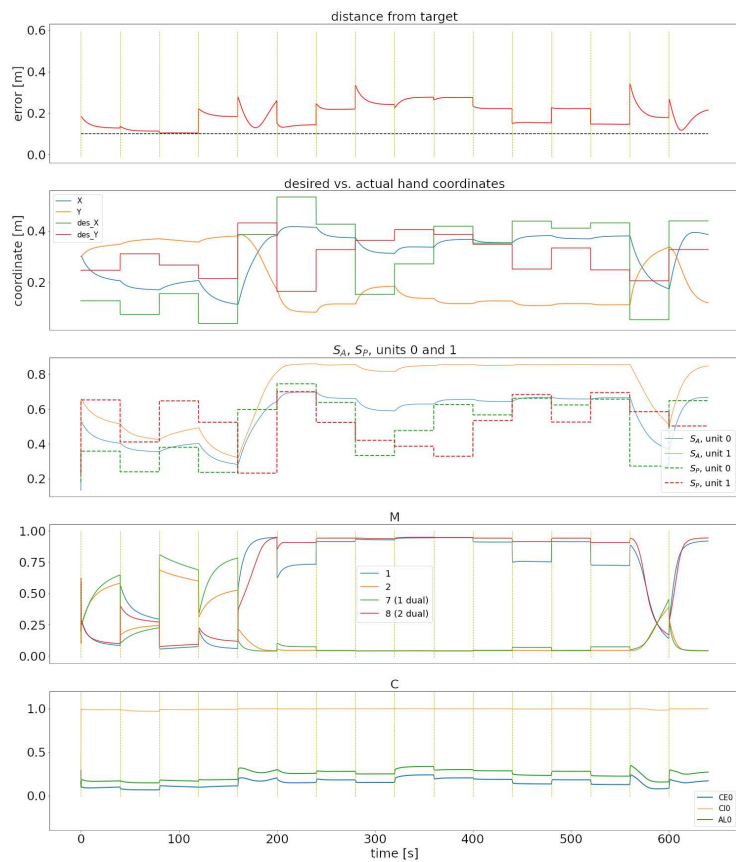


Figure S6: A failure to learn for a simulation of configuration 1 with no noise and no ACT unit. Captions are as in figure 2 of the main text.

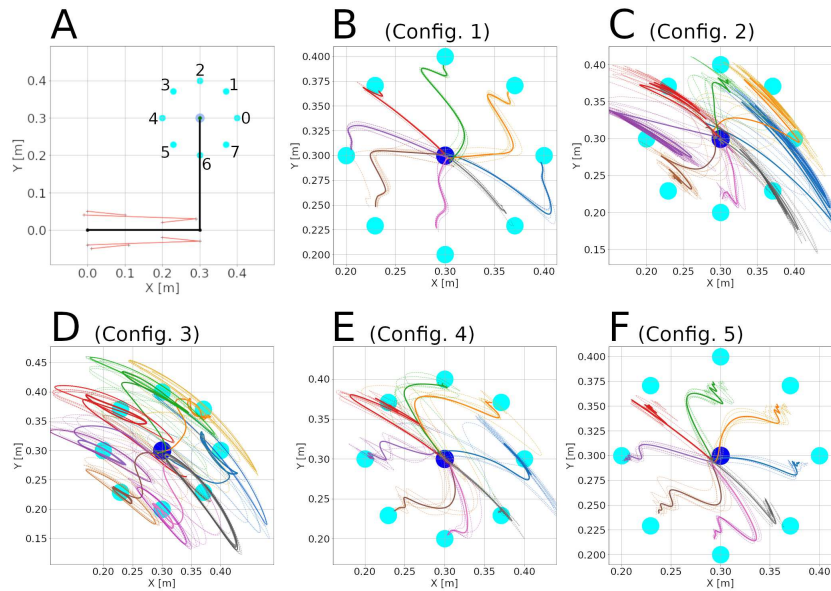


Figure S7: Center-out reaching before the control loop gain was adjusted. Panels are as in figure 3.

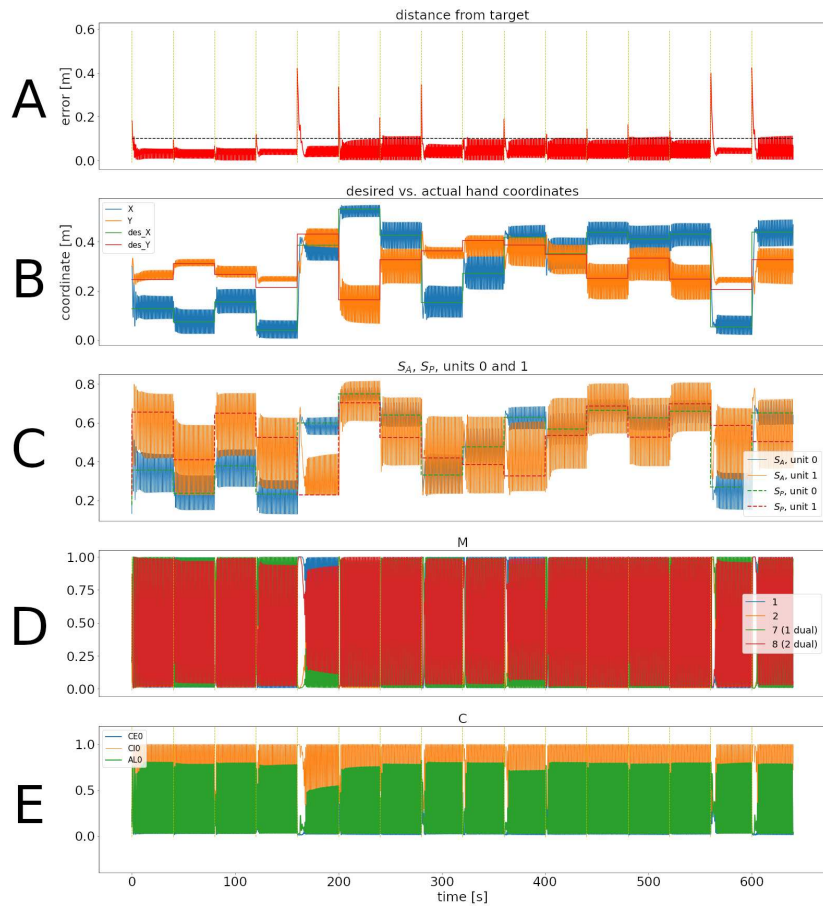


Figure S8: Training phase of the simulation for configuration 3 before gain was reduced. Panels are as in figure 2.

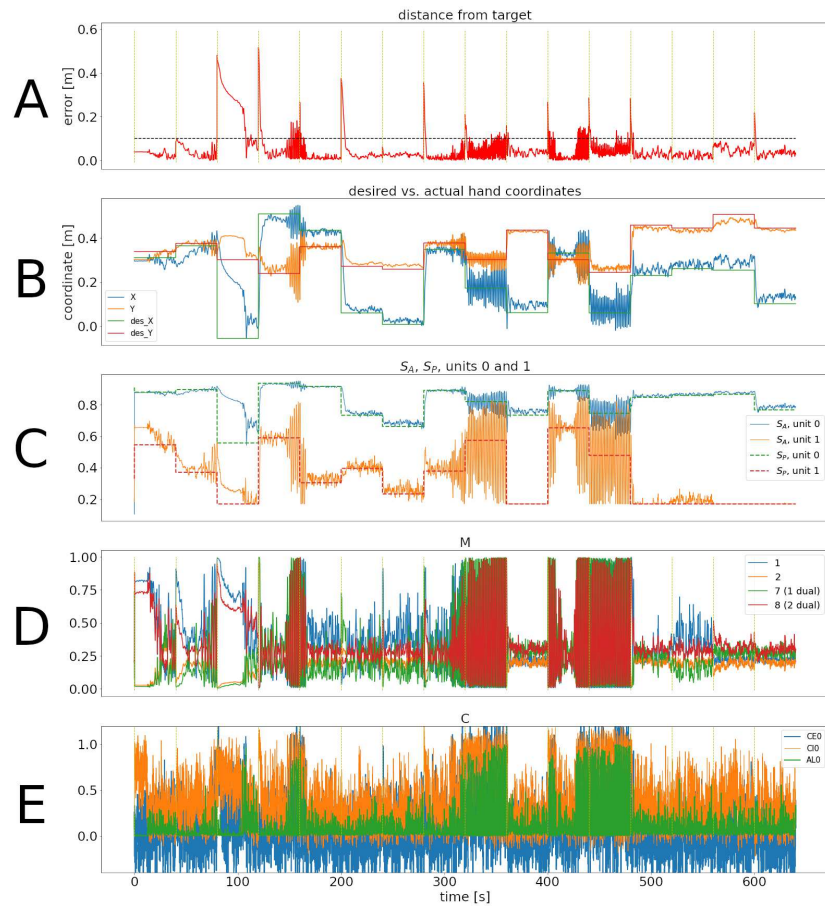


Figure S9: Training phase of the simulation for configuration 4 before gain was reduced. Panels are as in figure 2.